

Banner appropriate to article type will appear here in typeset article

# Suppression of Rayleigh-Bénard convection and restratification by horizontal convection

Florian Rein<sup>1</sup>†, Stefan G. Llewellyn Smith<sup>1,2</sup> and William R. Young<sup>1</sup>

<sup>1</sup>Scripps Institution of Oceanography, University of California San Diego, La Jolla CA 92093-0213, USA

<sup>2</sup>Department of Mechanical and Aerospace Engineering, Jacobs School of Engineering, University of California San Diego, La Jolla CA 92093-0411, USA

(Received xx; revised xx; accepted xx)

We investigate the competition between horizontal convection (HC) and Rayleigh-Bénard convection (RBC) in a fluid layer subject to a uniform destabilizing buoyancy flux at the bottom and a horizontally varying buoyancy distribution at the top. The RBC forcing imposes negative horizontal mean vertical buoyancy gradients at the top and bottom of the fluid layer. But if the HC forcing is sufficiently strong then the volume averaged vertical buoyancy gradient,  $\langle b_z \rangle$ , is positive i.e. opposite in sign to destabilizing RBC buoyancy gradients at the boundaries. If  $\langle b_z \rangle > 0$  we say that the layer has been “restratified”.

Using scaling analysis based on power integrals together with two-dimensional direct numerical simulations at Rayleigh numbers up to  $10^{10}$ , we identify two cases: a neutral stratification state, in which HC first offsets RBC so that  $\langle b_z \rangle = 0$ , and a strong stratification regime, in which HC dominates and  $\langle b_z \rangle$  is opposite in sign, and greater in magnitude, than the prescribed destabilizing vertical buoyancy gradient at the layer boundaries. For the range of parameters explored in this study, we derive scaling laws for the onset of these regimes in terms of the horizontal and vertical flux Rayleigh numbers,  $Ra_H$  and  $Ra_V$ , finding  $Ra_H^N \sim Ra_V^{4/5}$  for the neutral state and  $Ra_H^S \sim Ra_V$  for the onset of strong stratification. The results highlight the controlling role of the top boundary layer in setting the mean stratification and clarify the conditions under which HC suppresses RBC.

These findings are relevant to geophysical environments such as subglacial lakes, and the oceans of Snowball Earth and icy moons, where bottom heating and horizontal buoyancy variations jointly shape ocean stratification.

**Key words:** Rayleigh-Bénard convection, horizontal convection, geothermal heat flux, ice-covered satellites, Neoproterozoic Earth

---

† Email address for correspondence: florian.rein@protonmail.com

## 1. Introduction

Geothermal heating of the Earth’s oceans has a flux Rayleigh number of order  $10^{24}$  (see [Appendix A](#)). This strongly supercritical bottom heating does not result in Rayleigh-Bénard convection (RBC). Instead, ocean stratification is reliably stable – even strongly stable in the sense that the buoyancy frequency is greater than the Coriolis frequency almost everywhere. Suppression of geothermally forced RBC indicates the importance of horizontal convection (Rossby 1965, 1998; Hughes & Griffiths 2008) associated with a sea-surface pole-to-equator temperature difference of order 30 K. Horizontal convection (HC), assisted by wind and tides, produces a stably stratified ocean (Munk & Wunsch 1998). Impelled by observations of stable ocean stratification, oceanographers are concerned only with secondary effects of geothermal heating, such as modification of abyssal water masses (e.g. Emile-Geay & Madec 2009; De Lavergne *et al.* 2016) or the possibility that geothermal heating enhances the strength of the meridional overturning circulation (e.g. Mullarney, Griffiths & Hughes 2006; Wang, Huang, Zhou & Xia 2016).

We refer to the production of stable interior stratification in a bottom-heated fluid layer as “restratification.” As a definition, we say that the fluid is restratified if the volume average of the vertical buoyancy gradient –  $\langle b_z \rangle$  in the notation of section 2 – is positive. [Figure 1](#) shows an example of restratification: in the HC+RBC configuration the volume-averaged vertical buoyancy gradient  $\langle b_z \rangle$  is positive, despite bottom heating.

Geophysical convection problems involving restratification include the circulation of subglacial lakes (Thoma *et al.* 2009; Couston & Siegert 2021), the ocean of snowball Earth during the Neoproterozoic (Hoffman & Schrag 2002; Pierrehumbert *et al.* 2011) and the oceans of icy moons such as Europa and Enceladus (e.g. Soderlund 2019; Lemasquerier, Bierson & Soderlund 2023). In these systems geothermal heating is essential in maintaining a liquid ocean beneath an ice sheet. The ice sheet has variable thickness, and therefore variable pressure and freezing temperature at its base. The non-uniform basal ice temperature results in HC, and perhaps restratification, in the geothermally heated water below. Other horizontal non-uniformities result from spatial variations in the bottom flux of heat, salinity fluxes from the freezing and melting of ice, and non-uniform depth of the water layer.

The oceans of icy moons and of snowball Earth differ from Earth’s present ocean in that there is no sea-surface forcing by wind stress. Wind stress is the main source of energy for ocean circulation (Munk & Wunsch 1998; Wunsch & Ferrari 2004). It is likely therefore that the circulation of icy-moon oceans differs qualitatively from that of Earth: observations of ubiquitous statically stable stratification in Earth’s present ocean are not a reliable guide to stratification in other bottom-heated oceans.

Investigations of snowball Earth and icy moons make diverse and contradictory assumptions regarding the competition between RBC and HC in these systems. For example, Jansen (2016) assumes that horizontal inhomogeneities in snowball Earth heat fluxes result in statically stable stratification. In Jansen’s view, vertical heat fluxes, required to transmit geothermal heat to the base of the ice sheet, result from baroclinic instability (also known as slantwise convection) in a horizontally restratified ocean. On the other hand, Ashkenazy & Tziperman (2016) argue that the ocean of snowball Earth is, to a first approximation, well

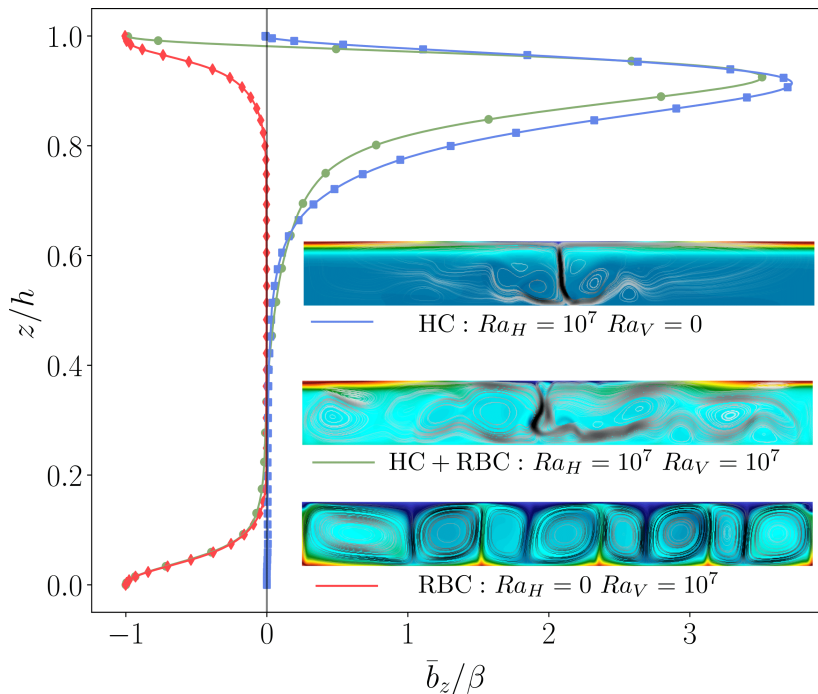


Figure 1: Horizontally- and time-averaged vertical buoyancy gradient  $\bar{b}_z(z)$  in three cases. The inset shows a snapshots of the buoyancy with overlaid streamlines. The HC Rayleigh number,  $Ra_H$ , and the RBC flux Rayleigh number,  $Ra_V$ , are defined in (2.7); other parameters are  $\Gamma = 8$  and  $Pr = 1$ . For the joint HC and RBC case, the time and volume-averaged vertical buoyancy gradient is  $\langle b_z \rangle / \beta = 0.38$ , where  $\beta > 0$  is defined in (2.1).

mixed vertically by geothermal RBC. In a numerical exploration of icy-moon ocean circulation, Bire *et al.* (2022) ignore horizontal inhomogeneities that might result in HC and focus instead on rotating RBC forced by unopposed uniform bottom heating. But in another exploration of icy-moon ocean circulation, Zhang *et al.* (2024) use an insulating bottom boundary condition (no RBC) and instead force with horizontally non-uniform temperature (i.e. HC) at the base of the ice sheet.

Models of icy-moon oceans are largely unconstrained by observations. For snowball Earth, ignorance is even more profound and likely to remain so. It is essential therefore to identify the parameters determining whether the bulk stratification  $\langle b_z \rangle$  of these oceans is statically stable. Subsequent modeling depends heavily on this issue. For example, a stably stratified ice-covered ocean might be energized by tidally generated internal waves resulting in turbulent interior mixing (e.g. Wunsch 2016). Baroclinic instability occurs only if the bulk stratification is stable. Sufficiently strong stable stratification is the basis for the “traditional approximation” in which the component of the Coriolis force along the direction of the base-state buoyancy gradient is neglected (e.g. Gerkema *et al.* 2008). In short, if  $\langle b_z \rangle > 0$  then business-as-usual ocean modeling can proceed. If  $\langle b_z \rangle < 0$  then a very different class of models, suggested by processes in a stellar convection zone, might be appropriate.

For both RBC and HC a key challenge is determining the relation between heat

transport and surface forcing, i.e. the relation between Nusselt  $Nu$  and Rayleigh  $Ra$  numbers. While the  $Nu$ - $Ra$  relation is not a goal of this investigation, related boundary-layer scaling arguments are useful in section 4. For the RBC boundary layer, see Grossmann & Lohse (2000, 2001), Doering (2020) and Lindborg (2023). For the HC boundary layer the literature is smaller: see Rossby (1965, 1998), Shishkina *et al.* (2016) and more recently Passaggia & Scotti (2024) and Passaggia *et al.* (2024).

Motivated by the dynamics of subglacial lakes, Coustou, Nandaha & Favier (2022) (hereafter CNF) investigated the competition between RBC and HC and demonstrated a regime transition between the two varieties of convection. Close to the regime transition, and with flux Rayleigh number as large as  $10^6$ , CNF showed that there is bistability and hysteresis: two stable flow states co-exist at the same parameter values. In one state RBC is dominant (multiple convection cells, most with a horizontal scale comparable to the layer depth) and in the other state HC dominates (fewer cells, most elongated in the horizontal direction). The history of the system determines which state is observed.

Here we use the RBC+HC setup studied by CNF, focusing on the issue of restratification. Restratification indicates that the competition between RBC and HC is settled: RBC has capitulated and most of the fluid is statically stable with  $\langle b_z \rangle$  having the positive sign characteristic of HC.

Geophysical situations present complications such as rotation, salinity, and spherical shell geometry. But understanding restratification in the idealized RBC+HC model is a necessary prerequisite: we must first identify the non-dimensional parameters that determine the outcome of this competition in the relatively simple RBC+HC model.

Section 2 presents the governing equations, numerical setup, and control parameters. We define the two Rayleigh numbers that quantify the bottom buoyancy flux and the horizontal buoyancy forcing. Section 3 defines restratification, and section 4 examines the flow phenomenology and key scalings of two characteristic stratification configurations: neutral and strong stratification. Section 5 develops scaling arguments based on the dynamics of the top boundary layer and identifies its controlling role in the system. We derive scaling laws for the boundary-layer thickness and mean buoyancy in the asymptotic regimes in which RBC dominates horizontal convection and vice versa. The same framework is then used to determine the thresholds for the onset of neutral and strong stratification, establishing their dependence on the flux and horizontal Rayleigh numbers in both low- and high-Rayleigh regimes. Section 6 examines the sensitivity of the results to variations in the Prandtl number, compares them with the findings of CNF, and explores the implications for geophysical systems where bottom heating and lateral buoyancy gradients interact. Section 7 concludes with directions for future work.

## 2. Formulation of the restratification problem

### 2.1. The Boussinesq equations

We consider a layer of Boussinesq fluid with depth  $h$  and density  $\rho = \rho_{\text{ref}}(1 - g^{-1}b)$ , where  $\rho_{\text{ref}}$  is a constant reference density,  $g$  is the gravitational acceleration and  $b$  is the ‘‘buoyancy’’. If, for example, the fluid is stratified by temperature variations then  $b = g\alpha(T - T_{\text{ref}})$ , where  $T_{\text{ref}}$  is a reference temperature,  $\alpha$  is the thermal

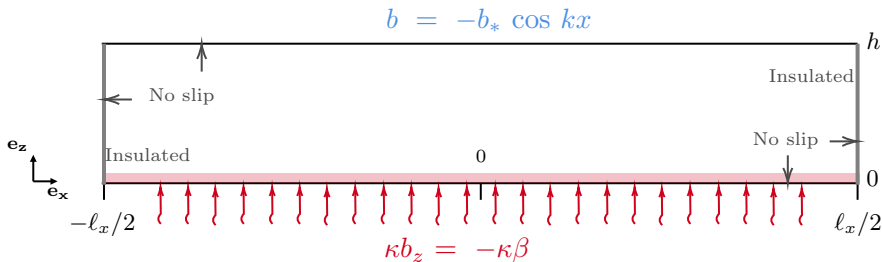


Figure 2: Sketch of the 2D fluid layer illustrating the boundary conditions. There is a uniform buoyancy flux,  $F = \kappa\beta$ , through the bottom, non-uniform buoyancy at the top and no buoyancy flux through the sidewalls. All boundaries satisfy no-slip velocity conditions.

expansion coefficient and  $g$  is the gravitational acceleration. We define  $T_{\text{ref}}$  so that the horizontal and time average of  $b$  prescribed at the top surface  $z = h$  is zero.

At the bottom,  $z = 0$ , the buoyancy boundary condition is specified constant diffusive flux of buoyancy,  $F$  defined in (A 4), into the fluid. This is equivalent to the Neumann boundary condition

$$b_z(x, y, 0, t) = -\beta, \quad (2.1)$$

where  $\beta = F/\kappa > 0$ . At the top of the layer,  $z = h$ , the boundary condition is

$$b(x, y, h, t) = b^s(x, y), \quad (2.2)$$

where the ‘‘surface buoyancy’’  $b^s$  is a specified function of position, e.g. (2.6) below.

With the notation above, the Boussinesq equations of motion are

$$\mathbf{u}_t + \mathbf{u} \cdot \nabla \mathbf{u} + \nabla p = b\hat{\mathbf{z}} + \nu \nabla^2 \mathbf{u}, \quad (2.3)$$

$$b_t + \mathbf{u} \cdot \nabla b = \kappa \nabla^2 b, \quad (2.4)$$

$$\nabla \cdot \mathbf{u} = 0. \quad (2.5)$$

The kinematic viscosity is  $\nu$  and the thermal diffusivity is  $\kappa$ . We impose no-slip boundary conditions on all solid boundaries. In two-dimensional numerical solutions, with  $-\ell_x/2 < x < +\ell_x/2$ , we use the sinusoidal profile

$$b^s(x) = -b_* \cos kx, \quad (2.6)$$

with  $k = 2\pi/\ell_x$ . In general one can introduce a buoyancy scale  $b_*$  as a dimensional measure of horizontal buoyancy variations specified at the top surface. We take  $b_* > 0$  so that the densest surface fluid is in the middle of the domain at  $x = 0$ . The HC plume is then well away from the no-slip sidewalls at  $x = \pm\ell_x/2$  (see inset in figure 1). This setup is illustrated in Figure 2.

Numerical solutions of (2.1) through (2.6) presented in section 4 and 5 are based on the two-dimensional (2D) case with  $\ell_y = 0$ . The theoretical developments in section 3, however, applies equally well to the three-dimensional (3D) case. And in section 6 we assess the effects of three-dimensionality by presenting numerical solutions with periodicity in the  $y$ -direction and  $\ell_y = h$ .

## 2.2. Non-dimensional control parameters

This problem is characterized by both a HC Rayleigh number and a vertical RB flux Rayleigh number:

$$\text{Ra}_\text{H} \stackrel{\text{def}}{=} \frac{h^3 b_\star}{\nu \kappa} \quad \text{and} \quad \text{Ra}_\text{V} \stackrel{\text{def}}{=} \frac{h^4 F}{\nu \kappa^2} = \frac{h^4 \beta}{\nu \kappa}. \quad (2.7)$$

Additional non-dimensional parameters are the Prandtl number and aspect ratio:

$$\text{Pr} \stackrel{\text{def}}{=} \frac{\nu}{\kappa} \quad \text{and} \quad \Gamma \stackrel{\text{def}}{=} \frac{\ell_x}{h}. \quad (2.8)$$

The traditional definition of the HC Rayleigh number, introduced by Rossby (1965, 1998), is based on the horizontal length  $\ell_x$  and the total difference between the maximum and minimum imposed surface buoyancy. In our notation, and using the sinusoidal surface buoyancy profile in (2.6), this traditional HC Rayleigh number is

$$\text{Ra}_\text{H}^{\text{trad}} = \frac{2b_\star \ell_x^3}{\nu \kappa} = 2\Gamma^3 \text{Ra}_\text{H}. \quad (2.9)$$

Our unconventional definition of  $\text{Ra}_\text{H}$  simplifies subsequent results. But because we consider largish aspect ratios ( $\Gamma \geq 8$ ) our  $\text{Ra}_\text{H}$  is smaller than the corresponding  $\text{Ra}_\text{H}^{\text{trad}}$  by a factor of at least  $2^{10}$ . This factor  $2^{10}$  complicates comparison of our results with earlier studies of HC using  $\text{Ra}_\text{H}^{\text{trad}}$  as a control parameter.

We introduce non-dimensional variables denoted by a dash and defined by

$$(x, y, z) = h(x', y', z'), \quad t' = \kappa t / h^2, \quad (2.10)$$

$$\mathbf{u}' = h\mathbf{u}/\kappa, \quad p' = h^2 p / (\nu \kappa), \quad b' = h^3 b / (\nu \kappa). \quad (2.11)$$

Dropping the dash, the non-dimensional versions of (2.3) through (2.5) are

$$\text{Pr}^{-1}(\mathbf{u}_t + \mathbf{u} \cdot \nabla \mathbf{u}) = -\nabla p + b \hat{\mathbf{z}} + \nabla^2 \mathbf{u}, \quad (2.12)$$

$$b_t + \mathbf{u} \cdot \nabla b = \nabla^2 b, \quad (2.13)$$

$$\nabla \cdot \mathbf{u} = 0. \quad (2.14)$$

The non-dimensional versions of the boundary conditions in (2.1) and (2.6) are

$$b(x, y, 1, t) = -\text{Ra}_\text{H} \cos kx, \quad b_z(x, y, 0, t) = -\text{Ra}_\text{V}. \quad (2.15)$$

The unconventional definition of non-dimensional variables in (2.10) and (2.11) ensures that Rayleigh numbers  $\text{Ra}_\text{H}$  and  $\text{Ra}_\text{V}$  appear on equal footing in the boundary conditions (2.15). Using  $\text{Ra}_\text{H}$ , rather than  $\text{Ra}_\text{H}^{\text{trad}}$ , ensures that the aspect ratio  $\Gamma$  does not appear in the boundary conditions (2.15).

The governing equations (2.12–2.14), together with the boundary conditions (2.15), and no-slip conditions on all boundaries, are solved numerically in a two-dimensional box using the spectral-element code [Nek5000](#) (Fischer 1997; Deville *et al.* 2002). This solver has been widely applied to studies of thermal convection (e.g. Scheel *et al.* 2013; Rein *et al.* 2023). Further details of the numerical method and its implementation are in [Appendix B](#).

Pure RBC corresponds to  $\text{Ra}_\text{H} = 0$ , or equivalently  $b_\star = 0$ . This is type 3 RBC as defined by Goluskin (2016): the lower boundary condition is fixed flux and the upper boundary condition is fixed uniform temperature. With  $b_\star = 0$  there is a motionless diffusive solution with  $\mathbf{u} = \mathbf{0}$  and  $b = \beta(h - z)$ . This solution is linearly unstable if  $\text{Ra}_\text{V} > 1295.78$  and is globally stable if  $\text{Ra}_\text{V} < 1295.78$

(Goluskin 2016). Type 3 RBC is cellular: at onset the most unstable horizontal wavenumber is  $kh = 2.5519$ .

Pure HC corresponds to  $\text{Ra}_V = 0$ . In HC the smallest temperature variation at  $z = h$  create horizontal pressure gradients that set the fluid into motion. i.e. the critical value of  $\text{Ra}_H$  is zero. In contrast to cellular RBC, HC produces overturning flow with a horizontal length scale determined by the applied surface buoyancy; see [Figure 1](#).

### 3. Definition of restratification

#### 3.1. Power integrals

We use an overbar to denote an average over  $x$ ,  $y$  and  $t$ , taken at any fixed  $z$ , e.g. see  $\bar{b}_z$  in [figure 1](#). Angle brackets  $\langle \rangle$  denote a total volume and time average. For [operational](#) details of the averaging process, see [Appendix B](#).

Forming  $\langle \mathbf{u} \cdot (2.3) \rangle$  produces the energy power integral

$$\varepsilon = \langle wb \rangle, \quad (3.1)$$

where  $\varepsilon \stackrel{\text{def}}{=} \nu \langle |\nabla \mathbf{u}|^2 \rangle > 0$  is the rate of dissipation of kinetic energy and  $\langle wb \rangle$  is the rate of conversion from internal and gravitational potential energy to kinetic energy.

Averaging the buoyancy equation [\(2.4\)](#) over the horizontal coordinates and time  $t$ , and then integrating in  $z$ , leads to the flux constraint

$$\overline{wb} - \kappa \bar{b}_z = \kappa \beta. \quad (3.2)$$

In pure HC, with  $\beta = 0$ , [\(3.2\)](#) is the zero-flux constraint of Paparella & Young (2002). With non-zero buoyancy flux through the bottom, [\(3.2\)](#) says that in steady state the same buoyancy flux  $\kappa\beta$  must pass through every level.

Taking the  $z$ -integral of [\(3.2\)](#), dividing by  $h$ , and substituting into [\(3.1\)](#) gives

$$\varepsilon = \kappa\beta + \kappa \langle b_z \rangle. \quad (3.3)$$

In [\(3.3\)](#)  $\varepsilon$  and  $\kappa\beta$  are both positive. But the third term,  $\kappa \langle b_z \rangle$ , might have either sign. From [\(2.4\)](#) we obtain the buoyancy power integral

$$\chi = \overline{\kappa b_z(h) b^s(x)} / h - \kappa \beta \langle b_z \rangle, \quad (3.4)$$

where  $\chi \stackrel{\text{def}}{=} \kappa \langle |\nabla b|^2 \rangle$  is the dissipation of buoyancy variance and  $b_z(h) = b_z(x, y, h, t)$  (e.g. Rocha *et al.* 2020; Winters & Young 2009). Although  $\chi$  is positive the terms on the right of [\(3.4\)](#) can have either sign.

#### 3.2. Neutral stratification, restratification, and strong restratification

In pure HC ( $F = \beta\kappa = 0$ ) it follows from [\(3.3\)](#) that  $\langle b_z \rangle > 0$ . The other limiting case is pure type 3 RBC, corresponding to  $b^s(x) = 0$  and  $F > 0$ . In this case [\(3.4\)](#) shows that  $\langle b_z \rangle < 0$ . To summarize:

$$\text{pure HC (3.3)} \quad \Rightarrow \quad \langle b_z \rangle > 0; \quad (3.5)$$

$$\text{pure RBC (3.4)} \quad \Rightarrow \quad \langle b_z \rangle < 0. \quad (3.6)$$

The results above, based on power integrals, motivate using the sign change of  $\langle b_z \rangle$  to define the onset of ‘‘restratification’’: we say that a bottom-heated layer with non-uniform surface temperature is restratified by HC if  $\langle b_z \rangle > 0$ .

At the onset of restratification, with

$$\langle b_z \rangle = 0, \quad (3.7)$$

we say that the layer has “neutral stratification”. Recalling that  $\bar{b}(h) = 0$ , the identity

$$\langle b_z \rangle = -\frac{\bar{b}(0)}{h} \quad (3.8)$$

shows that a neutrally stratified layer has  $\bar{b}(0) = 0$ .

From the HC extremum principle (Paparella & Young 2002), the smallest (most negative) buoyancy in the domain must be greater than the smallest buoyancy prescribed at the surface  $z = h$ . Hence for the sinusoidal surface profile in (2.6) we obtain from (3.8)

$$\langle b_z \rangle \leq \frac{b_\star}{h}. \quad (3.9)$$

Restating (3.9) in dimensionless variables produces an upper bound on the possible strength of restratification

$$\frac{\langle b_z \rangle}{\beta} \leq \frac{\text{Ra}_H}{\text{Ra}_V}. \quad (3.10)$$

As a definition of the situation in which HC dominates RBC we say that the layer is “strongly restratified” if

$$1 \leq \frac{\langle b_z \rangle}{\beta}, \quad (\text{definition of strong restratification}). \quad (3.11)$$

The upper bound in (3.10) shows that strong restratification is not possible if  $\text{Ra}_H/\text{Ra}_V < 1$ .

The bottom boundary condition is  $b_z(x, y, 0, t) = -\beta$ , so strong restratification means that the bulk stratification,  $\langle b_z \rangle$ , is equal in magnitude, but opposite in sign, to the destabilizing bottom buoyancy gradient. This definition of strong restratification is somewhat arbitrary. But solutions discussed in section 4 indicate that with (3.11) the top boundary layer is characteristic of HC, i.e. if inequality (3.11) applies then RBC has capitulated to HC.

Rotation does not alter the power integrals in (3.3) and (3.4). Thus the definitions of neutral and strong stratification, and all results based on power integrals, extend to rotating flows.

## 4. Phenomenology and the surface boundary layer

We describe the flow characteristics associated with neutral and strong restratification.

### 4.1. Neutral stratification

In the neutrally stratified state, with  $\langle b_z \rangle = 0$ , rising plumes generated by the bottom buoyancy flux are intermittently swept along the bottom towards the sidewalls by a large-scale horizontal circulation, as observed in CNF. This circulation is the bottom expression of the dominant HC overturning cell, which is in turn driven by the descending plume that forms near the centre of the upper

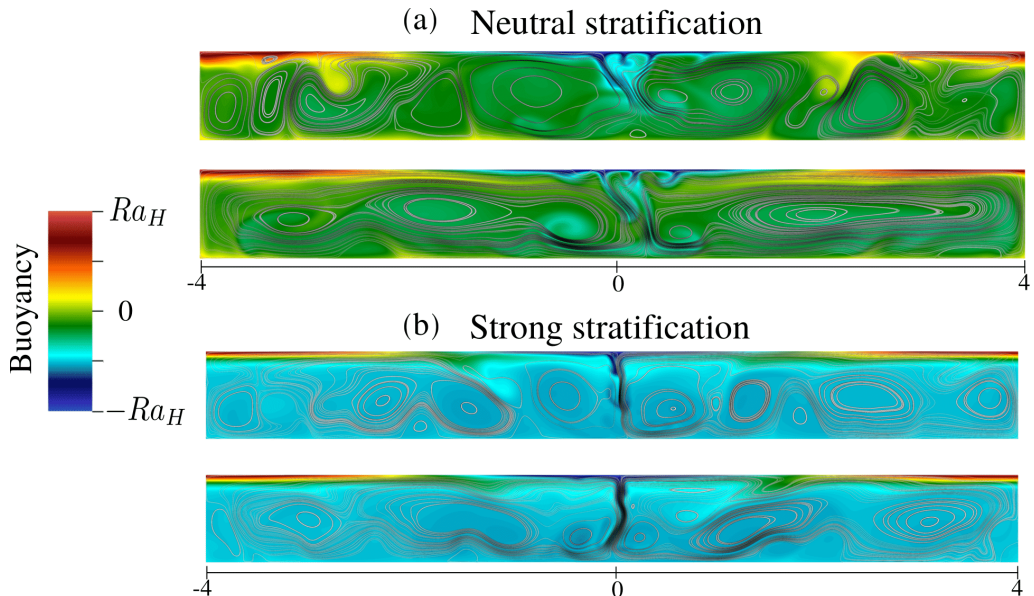


Figure 3: Two snapshots of the buoyancy field separated by a short time interval around  $0.02 h^2/\kappa$  for (a) the neutral stratification state ( $Ra_H = 3.35 \times 10^6$ ) and (b) the onset of the strong stratification regime ( $Ra_H = 2.03 \times 10^7$ ). Streamlines are overlaid in both cases. Parameters are  $Ra_V = 10^7$ ,  $\Gamma = 8$ , and  $Pr = 1$ . The buoyancy unit is  $\nu\kappa/h^3$ .

boundary. The flow alternates between RB-like convection cells and the broader HC circulation – see [Figure 3\(a\)](#).

Profiles of  $\bar{b}(z)$  with neutral stratification are shown in [Figure 4\(a\)](#). The buoyancy is normalized by the imposed HC surface amplitude  $b_*$ , and the vertical coordinate is rescaled by the thickness of the top boundary layer  $\delta$ , defined as the distance from the top boundary at which  $\bar{b}_z$  reaches 95% of its maximum value. When presented in this way,  $\bar{b}(z)$  profiles with  $Ra_V \geq 10^6$  collapse onto a common curve in the top boundary layer. Thus with  $\langle b_z \rangle = 0$ , the buoyancy variation across the top boundary layer is controlled by the imposed HC surface forcing  $b_*$ .

#### 4.2. Strong stratification

In the strong stratification regime RBC is largely suppressed: see [Figure 3\(b\)](#) and [Figure 4\(b\)](#) in which  $\langle b_z \rangle \approx +\beta$ , i.e. this is the onset of the strongly restatified regime. The horizontal bottom flow induced by the descending plumes at the top surface is sustained rather than intermittent. Some residual RBC effects remain, e.g. in [Figure 3\(b\)](#) weak upward plumes generated by the bottom flux are visible. These small RBC bottom plumes perturb the horizontal flow and enhance mixing near the bottom boundary compared to pure HC. The structure of this flow is primarily determined by HC but retains some influence of RBC, particularly near the heated bottom and the lateral edges.

Vertical profiles of the horizontally averaged buoyancy  $\bar{b}(z)$  for several values of  $Ra_V$  are shown in [Figure 4\(b\)](#). The buoyancy is normalized by the bottom forcing scale  $\beta h$ . As in the neutral case, the vertical coordinate is rescaled by the

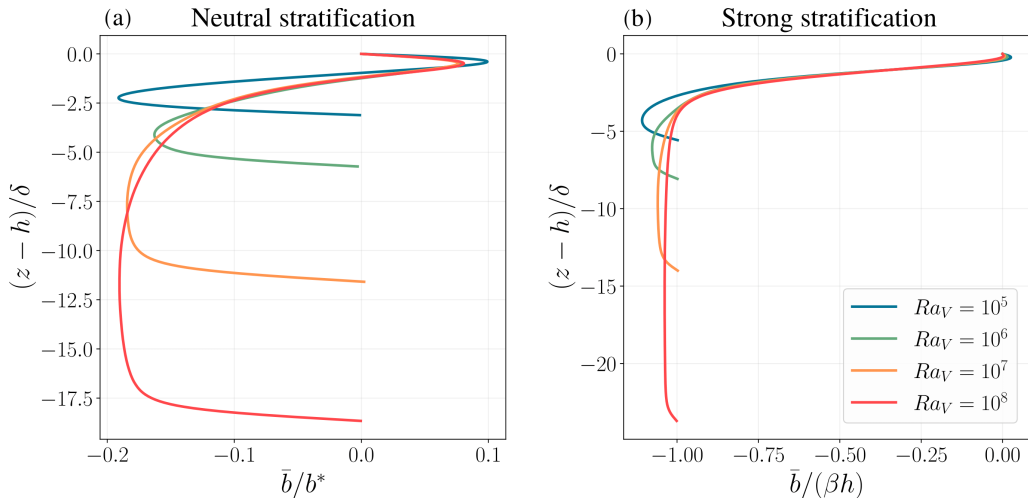


Figure 4: Vertical profile of the horizontal averaged buoyancy for several  $Ra_V$ , normalized by  $b_*$  in the neutral stratification regime in (a) and by  $\beta h$  in the strong stratification regime in (b). The boundary layer thickness  $\delta$  is computed from the vertical profile of  $\bar{b}_z(z)$  by determining the depth at which 95% of the maximum value of  $\bar{b}_z$  is reached. The parameters are  $\Gamma = 8$  and  $Pr = 1$ .

thickness of the top boundary layer  $\delta$ , defined as the depth at which  $\bar{b}_z$  reaches 95% of its maximum value.

In this strongly restratified regime, with  $\langle b_z \rangle \approx +\beta$ , the horizontally averaged buoyancy at the bottom is  $\bar{b}(0) = -\beta h$ . When normalized by  $\beta h$ ,  $\bar{b}(z)$  profiles collapse near the top boundary – see Figure 4(b) – indicating that the buoyancy variation across the top boundary layer is now controlled by  $\beta$  and confirming that this normalization of  $\bar{b}$  captures the structure of the top boundary layer at the onset of the strongly restratified state.

#### 4.3. Transition Rayleigh numbers

Consider a flow forced with a fixed value of  $Ra_V$ . If  $Ra_H = 0$  (pure RBC), then from (3.4)  $\langle b_z \rangle < 0$ . As  $Ra_H$  is increased from zero, the flow initially remains unchanged and continues to be dominated by RBC. With further increases in  $Ra_H$  the system undergoes a sharp transition: the convection pattern alternates between RBC cells and a large horizontal circulation driven by intermittent descending plumes from the upper boundary. This transition corresponds to the regime change identified and discussed by CNF. Further increasing  $Ra_H$  raises  $\langle b_z \rangle$ , and at some HC Rayleigh number, denoted  $Ra_H^N$ , the flow is neutrally stratified with  $\langle b_z \rangle = 0$ . With further increase in  $Ra_H$  the flow becomes strongly restratified at  $Ra_H^S > Ra_H^N$ . To precisely characterize these transitions we define the horizontal Rayleigh numbers corresponding to the neutral and strong stratification states respectively as

$$Ra_H^N(Ra_V, \Gamma, Pr) : \quad Ra_H \text{ at which } \langle b_z \rangle = 0, \quad (4.1)$$

$$Ra_H^S(Ra_V, \Gamma, Pr) : \quad Ra_H \text{ at which } \langle b_z \rangle = \beta. \quad (4.2)$$

Figure 5 shows the functions  $Ra_H^N$  and  $Ra_H^S$  in the  $(Ra_H, Ra_V)$  parameter space for  $Pr = 1$ ; we consider several aspect ratios as indicated. Each point in Figure 5

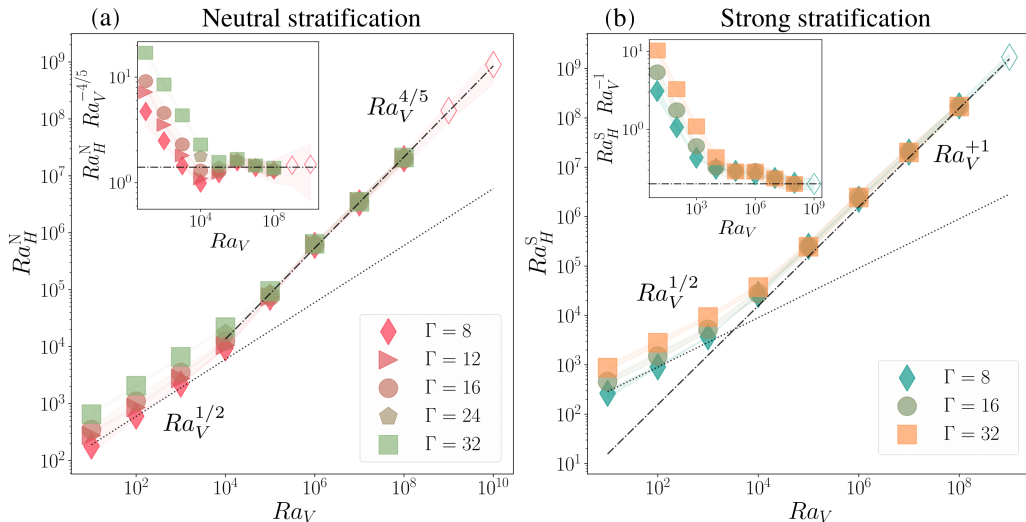


Figure 5: (a) Neutral horizontal Rayleigh number  $Ra_H^N$  (defined as the value of  $Ra_H$  for which  $\langle b_z \rangle = 0$  at a given  $Ra_V$ ) plotted as a function of  $Ra_V$  for several aspect ratios. The inset shows the same data compensated by the scaling law (5.10). For the two last  $Ra_V$  values ( $10^9, 10^{10}$ ), data are shown only for  $\Gamma = 8$ .

(b) Strong horizontal Rayleigh number  $Ra_H^S$  (defined as the value of  $Ra_H$  for which  $\langle b_z \rangle = \beta$  at a given  $Ra_V$ ) plotted as a function of  $Ra_V$  for several aspect ratios. The inset shows the same data compensated by the scaling law (5.14).

For the last  $Ra_V$  value ( $10^9$ ), data are shown only for  $\Gamma = 8$ . Empty/full symbols indicate respectively filtered/DNS simulations.

is determined using a bisection search: to determine  $Ra_H^N$  we fix  $Ra_V$ ,  $\Gamma$  and  $Pr$ . We then obtain a sequence of solutions in which the target  $Ra_H^N$  is bracketed and repeatedly halved until we located the value of  $Ra_H$  for which  $|\langle b_z \rangle / \beta| \leq 0.05$ . The shaded regions in Figure 5 indicate the uncertainty.

For low Rayleigh numbers ( $Ra_H, Ra_V \lesssim 10^4$ ), both neutral stratification and the onset of the strong stratification regime follow a power-law scaling

$$(Ra_H^N, Ra_H^S) \sim Ra_V^{1/2} \Gamma \quad (4.3)$$

with no dependence on  $Pr$ . Thus a main conclusion is that the neutral curve  $Ra_H = Ra_H^N(Ra_V, \Gamma, Pr)$  passes through the origin of the  $(Ra_V, Ra_H)$  parameter plane. Further detail and an analytic explanation of (4.3) are in Appendix C.

At higher Rayleigh numbers ( $Ra_H, Ra_V \gtrsim 10^4$ ), the system enters an aspect-ratio-independent regime, with

$$Ra_H^N(Ra_V, \Gamma, 1) \sim 8.54 Ra_V^{4/5}. \quad (4.4)$$

The onset of the strong stratification regime is at

$$Ra_H^S(Ra_V, \Gamma, 1) \sim 1.70 Ra_V. \quad (4.5)$$

The scaling above is consistent with the conclusion following (3.11) that strong restratification requires  $Ra_H > Ra_V$ .

The regimes in (4.4) and (4.5) are independent of aspect ratio  $\Gamma$ . This underscores the relevance of the layer thickness  $h$  as the characteristic length scale of the system and motivates the definition of  $Ra_H$  in (2.7) – using  $Ra_H^{\text{rad}}$  in (2.9)

introduces an artificial dependence on  $\Gamma$ . Figure 5(a) and (b) show our estimates of  $\text{Ra}_H^N$  and  $\text{Ra}_H^S$  at  $Pr = 1$  for different values of the aspect ratio  $\Gamma$ .

## 5. Scaling analysis

In this section, we analyze the system using scaling arguments, focusing on regimes where either RBC or HC dominates, as well as the neutral state with  $\langle b_z \rangle = 0$  and the onset of strong stratification at  $\langle b_z \rangle = +\beta$ . The horizontally-averaged buoyancy equation (3.2) shows that the buoyancy flux entering the domain through the bottom boundary layer must be conserved across any horizontal plane. Consequently, buoyancy must be extracted through a boundary layer at the top surface, leading to  $\bar{b}_z(h) = -\beta$ . Due to the imposed buoyancy profile at the top boundary, we expect this upper region to be the primary site where the competition between RBC and HC manifests itself, thereby governing the global dynamics of the system. We therefore focus on the structure and behavior of the top boundary layer.

Most of our numerical solutions use  $Pr = 1$  and we do not distinguish between viscous and buoyancy boundary layers. We assume that the characteristic vertical length scale is given by the thickness of the top boundary layer, denoted by  $\delta$ , such that  $\partial/\partial_z \sim 1/\delta$ . The characteristic horizontal length scale is taken to be  $\ell$ , which will be specified for each regime considered, implying  $\partial/\partial_x \sim 1/\ell$ .

We expect that a significant portion of both viscous and buoyancy dissipation is concentrated within the boundary layers (BLs), which occupy a fraction  $\delta/h$  of the domain. Accordingly, we estimate the dissipation rates as

$$\varepsilon = \nu \langle |\nabla \mathbf{u}|^2 \rangle \sim \nu \frac{U^2}{\delta^2} \left( \frac{\delta}{h} \right), \quad \chi = \kappa \langle |\nabla b|^2 \rangle \sim \kappa \frac{B^2}{\delta^2} \left( \frac{\delta}{h} \right), \quad (5.1)$$

where  $U$  is the characteristic horizontal velocity and  $B$  is the buoyancy difference across the top boundary layer, with the factor  $(\delta/h)$  coming from the ratio of the boundary layer thickness to the total depth.

From mass conservation (2.5), we obtain the relation  $U/\ell \sim W/\delta$ , where  $W$  is the characteristic vertical velocity within the top BL. Balancing advection with diffusion in the buoyancy equation (2.4) and this relation yields a scaling for the horizontal velocity

$$U \sim \frac{\kappa \ell}{\delta^2}. \quad (5.2)$$

### 5.1. Scalings in the asymptotic regimes

We now derive scaling laws for the top boundary layer thickness and mean buoyancy in two asymptotic regimes: when RBC dominates HC ( $\text{Ra}_V \gg \text{Ra}_H$ ), and when HC dominates RBC ( $\text{Ra}_H \gg \text{Ra}_V$ ).

#### 5.1.1. RBC-dominated regime

When the flux Rayleigh number greatly exceeds the horizontal Rayleigh number ( $\text{Ra}_V \gg \text{Ra}_H$ ), the dynamics are controlled by RBC. The horizontal length scale is set by the depth of the layer,  $\ell \sim h$ , and the imposed bottom buoyancy flux dominates the surface forcing. In this limit the power integrals (3.3)–(3.4) reduce to

$$\varepsilon \approx \kappa \beta \quad \text{and} \quad \chi \approx -\kappa \beta \langle b_z \rangle. \quad (5.3)$$

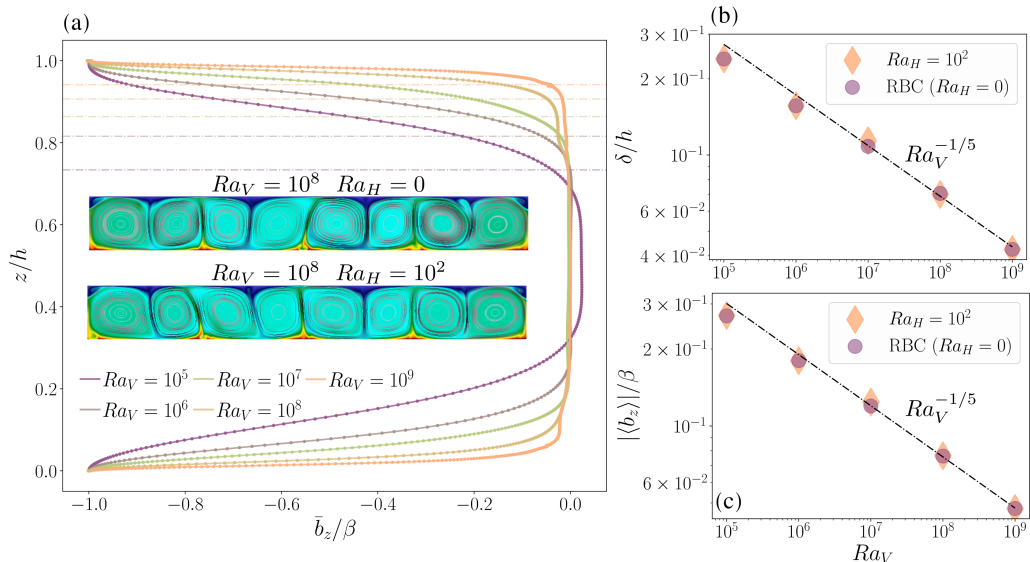


Figure 6: Vertical profiles of the mean vertical buoyancy gradient,  $\bar{b}_z$ , for varying  $Ra_V$  with fixed  $Ra_H = 10^2$  in panel (a). Dash-dot lines indicate the estimated thickness of the top boundary layer. Insets show snapshots of the buoyancy field: in (a), for pure RBC (top,  $Ra_V = 10^8$ ) and a mixed case (bottom,  $Ra_V = 10^8$ ,  $Ra_H = 10^2$ ). Panel (b) shows the boundary layer thickness  $\delta$  as a function of  $Ra_V$  for both pure RBC and mixed case. Panel (c) shows the norm of the mean vertical buoyancy gradient,  $|\langle b_z \rangle|$ , and its dependence on  $Ra_V$  for both pure RBC and mixed cases.

Assuming  $\langle b_z \rangle \sim B/h$ , i.e.  $(B/\delta)$  times the global average factor  $(\delta/h)$  and substituting the dissipation scalings (5.1) into (5.3) yields

$$\delta \sim hRa_V^{-1/5}, \quad B \sim \beta\delta \sim \beta hRa_V^{-1/5}. \quad (5.4)$$

These scalings are the fixed-flux equivalent of the regime-I scalings of Grossmann & Lohse (2000) for fixed-temperature boundaries, namely  $\delta \sim hRa_{\Delta b}^{-1/4}$ , where  $Ra_{\Delta b}$  is the classical RBC parameter based on the buoyancy difference  $\Delta b$  between the top and bottom plate. Adapting  $Ra_{\Delta b}^{-1/4}$  to an imposed bottom flux using  $\Delta b \approx \beta\delta$  gives  $Ra_{\Delta b} = (\delta/h)Ra_V$  (Otero *et al.* 2002; Johnston & Doering 2009), which then recovers (5.4) for the boundary-layer thickness.

The predicted trends are confirmed in Figure 6(b) and (c). Profiles of  $\bar{b}_z$  (panel a) show the definition of the top boundary-layer thickness  $\delta$ , taken as the distance from the top where  $\bar{b}_z$  falls to 95% of its maximum. In these panels, we present data from pure RBC simulations at  $Ra_V = 10^8$  and from a mixed-forcing case with  $Ra_V = 10^8$  and  $Ra_H = 10^2$ . For the mixed case with  $Ra_V = 10^8$  and  $Ra_H = 10^2$ , the data for both  $\delta$  and  $|\langle b_z \rangle|$  collapse onto those from pure RBC, indicating that the dynamics remain governed by RBC, with the horizontal forcing being too weak to produce any significant modification (see inset in Figure 6(a)).

### 5.1.2. HC-dominated regime

When the horizontal Rayleigh number is much larger than the flux Rayleigh number ( $Ra_H \gg Ra_V$ ), the flow is governed by HC. The relevant horizontal scale is that of the imposed surface buoyancy profile,  $\ell \sim \ell_x$ , and the surface forcing

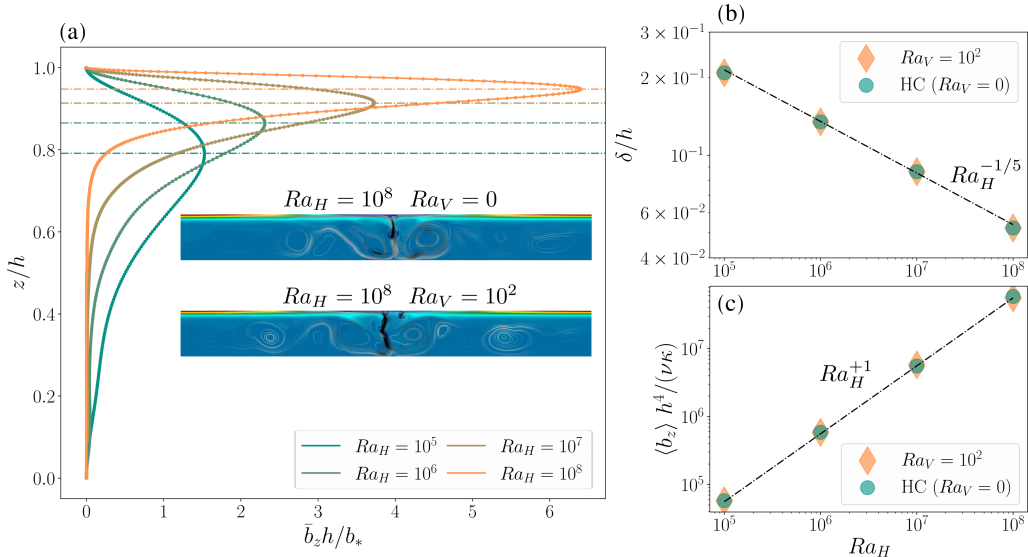


Figure 7: Vertical profiles of the mean vertical buoyancy gradient,  $\bar{b}_z$ , for varying  $Ra_H$  with fixed  $Ra_V = 10^2$  in panel (a). Dash-dot lines indicate the estimated thickness of the top boundary layer. Insets show snapshots of the buoyancy field for pure HC (top,  $Ra_H = 10^8$ ) and a mixed regime (bottom,  $Ra_H = 10^8$ ,  $Ra_V = 10^2$ ). Panel (b) shows the boundary layer thickness  $\delta$  as a function of  $Ra_H$  for both pure HC and mixed regime. Panel (c) shows the mean vertical buoyancy gradient  $\langle b_z \rangle$ , and its dependence in  $Ra_H$  for both pure HC and mixed regimes.

overwhelms the bottom flux. In this limit the power integrals reduce to

$$\varepsilon \approx \kappa \langle b_z \rangle, \quad \chi \approx \frac{\kappa}{h} \overline{b_z(h) b^s(x)}. \quad (5.5)$$

Using the dissipation estimates (5.1) gives

$$\delta \sim \ell_x (Ra_H \Gamma^3)^{-1/5}, \quad B \sim b_* \sim \frac{\nu \kappa}{h^3} Ra_H. \quad (5.6)$$

The explicit dependence on aspect ratio  $\Gamma$  reflects the fact that the HC Rayleigh number is naturally defined with the horizontal scale,  $Ra_{\ell_x} = Ra_H \Gamma^3$ . These scalings coincide with the classical HC results of Rossby (1965); see also the review of Hughes & Griffiths (2008).

The agreement with numerical solutions is shown in Figure 7(b) and (c). In these panels, we show data from pure HC simulations at  $Ra_H = 10^8$  and from a mixed-forcing case with  $Ra_H = 10^8$  and  $Ra_V = 10^2$ . For the mixed case, the measured  $\delta$  and  $|\langle b_z \rangle|$  collapse onto those from pure HC, indicating that the weak bottom forcing produces no measurable departure from HC behaviour (see inset of Figure 7(a)).

## 5.2. Neutral stratification state

Having examined the asymptotic regimes dominated by either RBC or HC, we now turn to the intermediate case corresponding to neutral stratification, defined by  $\langle b_z \rangle = 0$ . We adopt the same scaling approach as in the asymptotic regimes. In this transitional state, where neither forcing clearly dominates, the characteristic

horizontal length scale is expected to scale with the domain height, i.e.  $\ell \sim h$ . Importantly, with the condition  $\langle b_z \rangle = 0$ , the power integrals (3.3) and (3.4) simplify to two-term expressions:

$$\varepsilon = \kappa\beta \quad \text{and} \quad \chi = \frac{\kappa}{h} \overline{b_z(h) b^s(x)}. \quad (5.7)$$

Reflecting the mixed nature of the neutral stratification state,  $\varepsilon$  has the same expression as in the RBC-dominated regime (5.3), while  $\chi$  has the HC- form in (5.5). Substituting the dissipation scalings from (5.1) into (5.7) yields the following relations for the top boundary layer thickness and buoyancy jump:

$$\delta \sim h \text{Ra}_V^{-1/5}, \quad B \sim b_\star \sim \frac{\nu\kappa}{h^3} \text{Ra}_H. \quad (5.8)$$

Thus, the BL thickness follows the RBC scaling, while the buoyancy difference across the BL follows the HC scaling. Moreover the scaling for the buoyancy jump is consistent with Figure 4(a). However, since the net buoyancy flux must exit through the top boundary layer, the horizontally averaged buoyancy equation (3.2) still imposes the condition  $\bar{b}_z \approx -\beta$ . Using this, along with the scaling  $\bar{b}_z \sim b_\star/\delta$ , we obtain:

$$b_\star \sim \beta\delta. \quad (5.9)$$

Multiplying both sides of (5.9) by  $h^4/(\nu\kappa)$  and substituting the expression for  $\delta$  from (5.8) leads to the following relation:

$$\text{Ra}_H^N \sim \text{Ra}_V^{4/5}. \quad (5.10)$$

This scaling is in excellent agreement with the transition identified in Figure 5(a), thereby confirming the theoretical prediction.

### 5.3. The onset of strong stratification

We now consider the onset of the strong stratification, defined by the condition that  $\langle b_z \rangle = +\beta$ , i.e. the global stratification is equal in magnitude, but opposite in sign, to  $\bar{b}_z$  at the top and bottom of the layer. In this regime, HC is expected to dominate the dynamics, although not fully, meaning the characteristic horizontal length scale remains set by the domain height,  $\ell \sim h$ , rather than the imposed surface scale  $\ell_x$  (see Figure 3).

With  $\langle b_z \rangle = +\beta$  the power integrals (3.3) and (3.4) simplify to:

$$\varepsilon = 2\kappa\beta, \quad \text{and} \quad \chi = \frac{\kappa}{h} \overline{b_z(h) b^s(x)} - \kappa\beta^2. \quad (5.11)$$

As in the neutral regime,  $\varepsilon$  follows the RBC scaling (5.3), while the buoyancy variance dissipation  $\chi$  includes contributions from both RBC and HC. Substituting the dissipation scalings from (5.1) into (5.11) yields the following expressions for the top boundary layer thickness and buoyancy jump:

$$\delta \sim h \text{Ra}_V^{-1/5}, \quad B \sim b_\star - \frac{\beta^2 \delta h}{B}. \quad (5.12)$$

The boundary layer thickness continues to follow the RBC scaling in (5.8), while the buoyancy jump  $B$  is modified by a combination of HC and RBC effects. Because  $\langle b_z \rangle = \beta$  and  $\langle b_z \rangle \sim B/h$ , it follows that  $B \sim \beta h$ , in agreement with the scaling shown in Figure 4(b). Substituting  $B \sim \beta h$  into the expression for  $B$  in

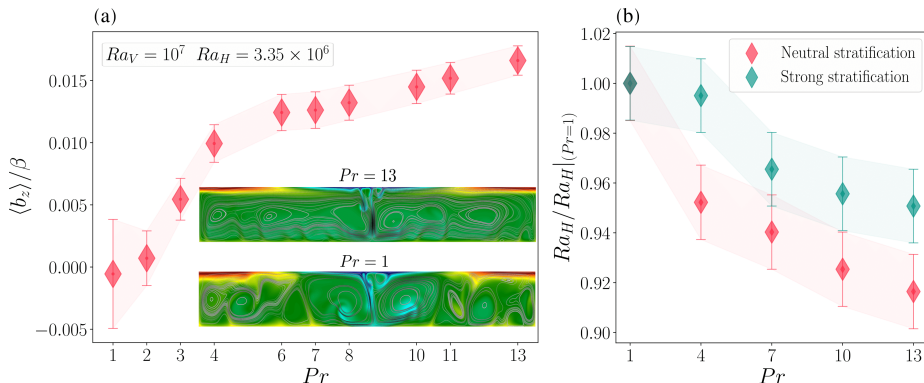


Figure 8: (a) Volume-averaged vertical buoyancy gradient, normalized by the imposed bottom flux  $\beta$ , as a function of the Prandtl number at the neutral state ( $Ra_H = 3.35 \times 10^6$ ). Insets show snapshots of the buoyancy field for  $Pr = 13$  (top) and  $Pr = 1$  (bottom). Error bars and the shaded region indicate one standard deviation about the temporal mean. (b) Neutral and strong horizontal Rayleigh numbers, each normalized by their value at  $Pr = 1$ , plotted versus the Prandtl number. Error bars and the shaded region indicate the uncertainty. All data correspond to  $Ra_V = 10^7$  and  $\Gamma = 8$ .

(5.12) leads to

$$b_* \sim \beta h \left( 1 + \frac{\delta}{h} \right). \quad (5.13)$$

Multiplying both sides of (5.13) by  $h^3/(\nu\kappa)$  and using the RBC scaling for  $\delta$  from (5.8), we obtain the following scaling:

$$Ra_H^S \sim Ra_V \left( 1 + Ra_V^{-1/5} \right). \quad (5.14)$$

The relation above reveals two distinct contributions to  $Ra_H^S$ : a dominant term proportional to  $Ra_V$  and a correction scaling with  $Ra_V^{4/5}$ . In the asymptotic limit  $Ra_V \gg 1$ , the leading-order behavior is  $Ra_H^S \sim Ra_V$ . This scaling is in agreement with the transition identified in Figure 5(b).

The scaling arguments above apply to the regime in which the flow remains boundary-layer dominated (regime I of Grossmann & Lohse (2000)). At higher Rayleigh numbers, transitions to different regimes of convection and associated changes in the Nusselt–Rayleigh scaling are expected. These will likely modify the  $Ra_H^N$  and  $Ra_H^S$  scalings above.

## 6. Discussion

### 6.1. Sensitivity to Prandtl number

Computations in the previous sections used  $Pr = 1$ . But the Prandtl number of water in icy-moon conditions is in the range 10 to 13. Figure 8(a) shows the variation of  $\langle b_z \rangle / \beta$  with increases in  $Pr$ . Starting from the neutral stratification regime at  $Ra_V = 10^7$  ( $Ra_H = Ra_H^N = 3.35 \times 10^6$ ) and  $(\Gamma, Pr) = (8, 1)$  we increase  $Pr$  with both Rayleigh numbers fixed. For each case, the system is evolved to a statistically steady state, and  $\langle b_z \rangle$  is computed by averaging over at least one diffusive time.

Increasing  $Pr$  enhances restratification: at  $Pr = 13$ ,  $\langle b_z \rangle / \beta = 0.015$ . The insets in **Figure 8(a)** show that at  $Pr = 13$  the flow exhibits features closer to the strong stratification regime e.g. convection cells are further suppressed and bottom plumes are weakened. **Figure 8(b)** shows the dependence of  $Ra_H^N$  and  $Ra_H^S$  on  $Pr$ . Increasing  $Pr$  lowers both  $Ra_H^N$  and  $Ra_H^S$  i.e. at larger  $Pr$  a weaker horizontal buoyancy forcing is required to attain  $Ra_H^N$  and  $Ra_H^S$  at fixed  $Ra_V$ . But the effect is small: between  $Pr = 1$  and  $Pr = 13$ ,  $Ra_H^N$  decreases by only about 10% and  $Ra_H^S$  by roughly 5%. Although this decrease in  $Ra_H^N$  and  $Ra_H^S$  is modest, we conclude that increasing  $Pr$  increases restratification by HC.

The dependence of the neutral transition on  $Pr$  may vary outside the moderate range considered here ( $1 \leq Pr \leq 13$ ), where different transport regimes are expected in both RBC (Grossmann & Lohse 2001; Lindborg 2023) and HC (Shishkina *et al.* 2016; Passaggia & Scotti 2024; Passaggia *et al.* 2024). Within the range  $1 \leq Pr \leq 13$ , we interpret the observed trend qualitatively in terms of boundary-layer structure: increasing  $Pr$  thins the buoyancy boundary layer relative to the viscous boundary layer, reducing the buoyancy contrast across it and hence the horizontal forcing required to attain neutral stratification.

## 6.2. Comparison with CNF

CNF's configuration differs from ours in two respects. Their half-wavelength sinusoidal surface forcing produces a single HC cell, whereas our full wavelength sinusoidal forcing in (2.6) results in two counter-rotating HC cells. Second, our HC plume does not interact with the no-slip sidewalls of the domain, whereas CNF's plume does. In pure HC this second difference produces a compact recirculating eddy associated with the HC plume; e.g. see CNF figure 2(f). This recirculating eddy is obtained in our configuration by making the sign of  $b_*$  in (2.6) negative, equivalently  $Ra_H < 0$ . Quantifying the effect, if any, of  $Ra_H < 0$  on restratification is beyond the scope of this work.

Fixing  $Ra_V$ , and varying an analog of  $Ra_H$ , CNF observed an interesting phenomenology involving the transient interruption of cellular RBC by episodic "bursts" of HC. CNF identify bursting as characteristic of the transition between an RBC regime and an HC regime. This identification of the RBC-HC transition differs from our  $\langle b_z \rangle = 0$  criterion for restratification.

**Figure 9** shows a solution in our configuration exhibiting HC bursting. The main point is that the time series of the instantaneous volume average  $b_z$  is always negative: see **Figure 9(a)**. In other words, as  $Ra_H$  is increased, with fixed  $Ra_V$  the system first enters the bursting regime, and then, at higher  $Ra_H$ , restratification occurs.

The CNF bursts occupy the entire horizontal extent of the domain. But here, because of full-wavelength surface forcing, bursts of HC occur independently in either half of the domain: see **Figure 9 (c) (d) and (e)**. During these bursts of HC, the flow carries a significant horizontal buoyancy flux: see **Figure 9(b)**. The volume-averaged of  $b_z$  in **Figure 9(a)** seems unaffected by this episodic horizontal buoyancy flux.

Louis-Alexandre Couston (personal communication) notes that in the single-cell configuration of CNF, HC bursts also occur with  $\langle b_z \rangle < 0$ . Summary: bursting is a first indication that HC is challenging RBC, but further increase in  $Ra_H$  is required for restratification.

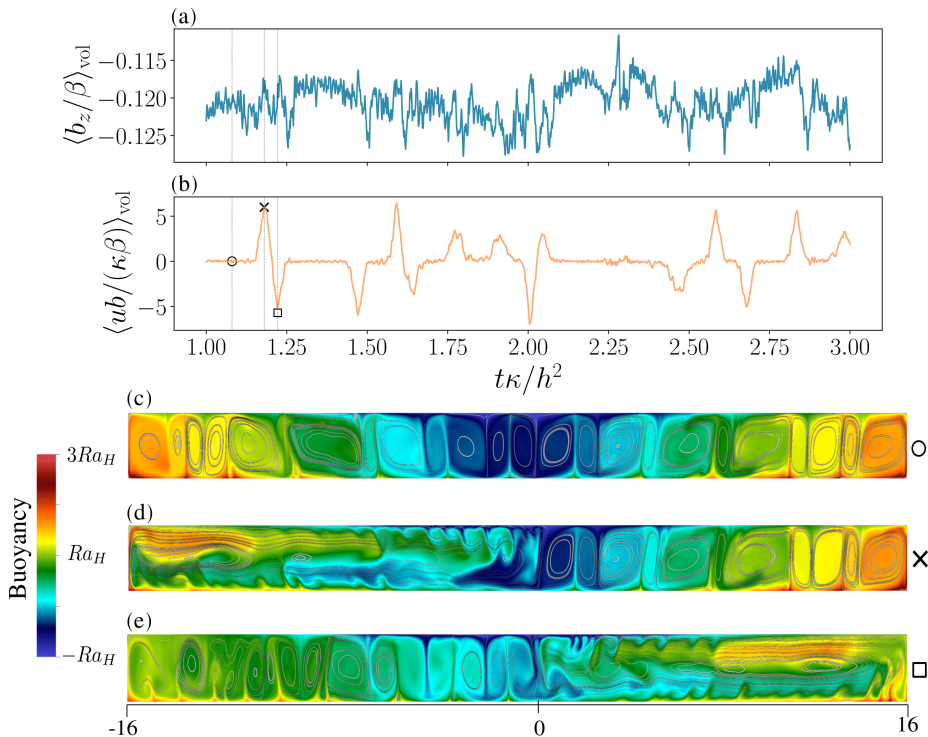


Figure 9: Time evolution of volume-averaged quantities (denoted  $\langle \cdot \rangle_{\text{vol}}$ ): (a)  $\langle ub \rangle_{\text{vol}}/(\kappa\beta)$ , and (b)  $\langle b_z \rangle_{\text{vol}}/\beta$ . Panels (c), (d) and (e) show snapshots (corresponding to times indicated in panel (b)) of the buoyancy field. The bulk stratification is unstable with  $\langle b_z \rangle/\beta = -0.121$ . Parameters are  $(Ra_H, Ra_V) = (10^6, 10^7)$  and  $(\Gamma, Pr) = (32, 1)$ .

### 6.3. Three-dimensionality: through thick and thin

Convection can differ significantly between two and three dimensions. In particular, the HC sweeping mechanism associated with the onset of the neutral state may be modified in 3D. Furthermore, while the inverse cascade of 2D turbulence promotes the formation of large-scale coherent structures, 3D flows exhibit a direct cascade of kinetic energy towards smaller scales and enhanced viscous dissipation.

To assess these effects, we undertook additional 3D simulations with periodic boundary conditions in the transverse  $y$ -direction. 2D solutions correspond to  $\ell_y = 0$ . With  $\ell_y = h/16$  (a ‘thin’ 3D domain) the numerical solution evolves to become independent of  $y$  and remains so; i.e. this thin 3D solution is statistically identical to the corresponding 2D solution with  $\ell_y = 0$ . Once the thin 3D solution reaches a statistically steady state we use a single-time snapshot as a 2D initial condition for a ‘thick’ 3D numerical solution with  $\ell_y = h$ . The thick 3D numerical solution is explosively unstable to transverse 3D disturbances and evolves into a complex eddying 3D flow. (We did not attempt to determine the critical value of  $\ell_y$  that triggers ‘three-dimensionalization’.)

Figures 10 and 11 compare the evolution of the thick 3D solution ( $\ell_y = h$ ) to a thin ( $\ell_y = h/16$ ) neutral ( $\langle b_z/\beta \rangle \approx 8.9 \times 10^{-4}$ ) solution. Activation of the third dimension decreases the kinetic energy by about 40% (figure 10(a)). The mean

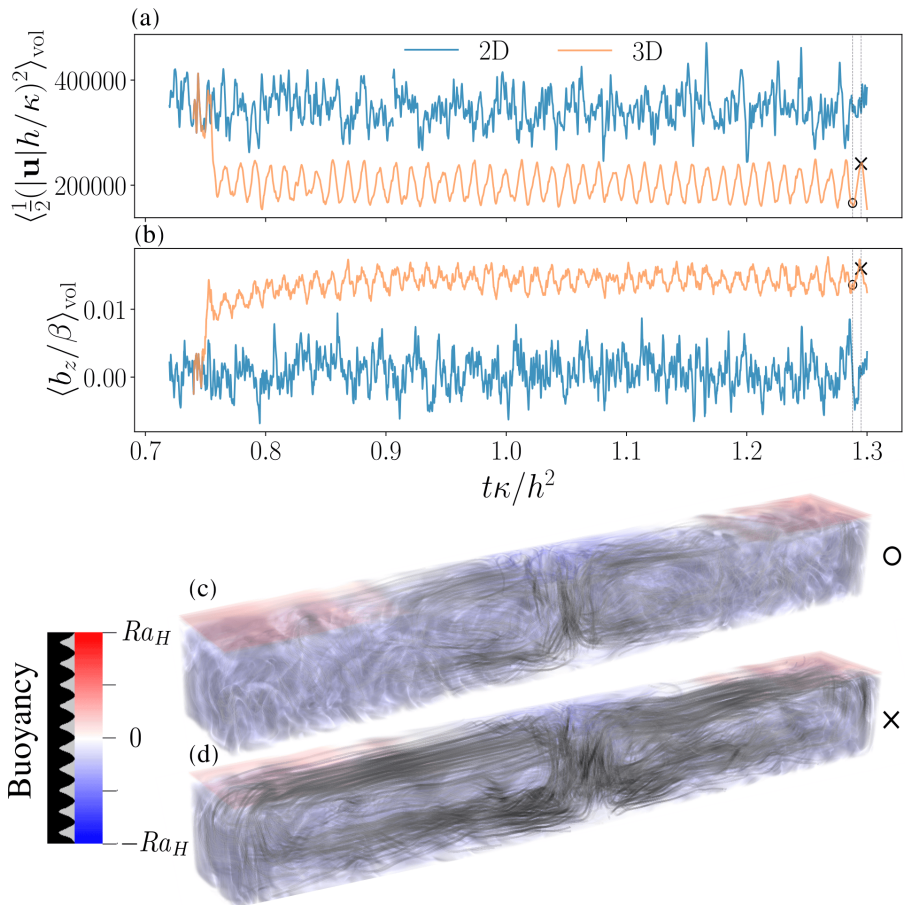


Figure 10: Time evolution of volume-averaged quantities: (a) kinetic energy and (b)  $\langle b_z/\beta \rangle_{\text{vol}}$ . Results from a 2D simulation are shown in blue, and the continuation of this case in 3D in orange. Panels (c) and (d) show snapshots of the buoyancy field at the times indicated in panel (a), with streamlines overlaid (colour scale and opacity shown in the colour bar). The bulk stratification is stable with  $\langle b_z \rangle/\beta = 1.45 \times 10^{-2}$ . Parameters are  $(Ra_H, Ra_V) = (0.2, 1) \times 10^8$  and  $(\Gamma, Pr) = (8, 1)$ .

stratification increases slightly, with  $\langle b_z \rangle$  rising to about  $0.015\beta$  (figure 10(b)). The viscous power integral

$$\varepsilon = \kappa\beta + \kappa\langle b_z \rangle, \quad (6.1)$$

indicates that with fixed  $\beta$  an increase in  $\langle b_z \rangle$  must be accompanied by an increase in viscous dissipation  $\varepsilon$ . This increase in  $\varepsilon$  is masked, however, by large fluctuations in the  $\varepsilon_{\text{vol}}(t)$  time series: see Figure 11(a). The 3D flow also has approximately 15% larger buoyancy variance dissipation  $\chi$  than that of the 2D comparison flow (Figure 11(b)). From the buoyancy variance power integral (3.4), for fixed  $\beta$  this increase in  $\chi$  requires an increase of the surface correlation term  $b_z(h)b^s(x)/h$  sufficient to compensate for the larger mean stratification  $\langle b_z \rangle$ .

The time series from the 3D solution in Figure 10 has striking oscillatory behaviour. This noisy periodicity is particularly clear in the kinetic energy time series in Figure 10(a). These oscillations are associated with the main descending

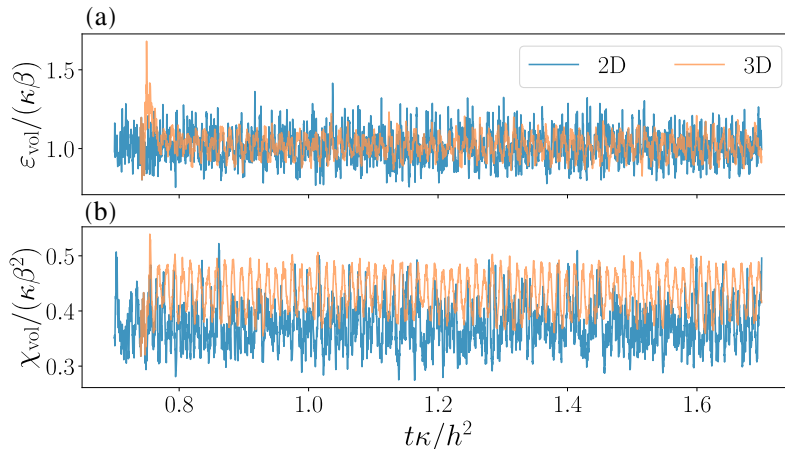


Figure 11: Time evolution of volume-averaged quantities: (a)  $\varepsilon_{\text{vol}}/(\kappa\beta)$  and (a)  $\chi_{\text{vol}}/(\kappa\beta^2)$  where  $\varepsilon_{\text{vol}} = \nu\langle|\nabla\mathbf{u}|^2\rangle_{\text{vol}}$  and  $\chi_{\text{vol}} = \kappa\langle|\nabla b|^2\rangle_{\text{vol}}$ . Results from an effectively 2D simulation ( $\ell_y/h = 1/8$ ) are shown in blue, and the continuation of this case in 3D ( $\ell_y/h = 1$ ) in orange. Parameters are  $(\text{Ra}_H, \text{Ra}_V) = (0.2, 1) \times 10^8$  and  $(\Gamma, Pr) = (8, 1)$ .

central plume and its associated large-scale cellular return flow that sweeps small bottom rising plumes towards the lateral boundaries (see [Figure 10\(c\)](#) and [\(d\)](#)). In the high kinetic energy state, denoted by  $\times$  in [Figure 10](#), the domain scale HC cells on either side of the central plume occupy the whole domain. In the low kinetic energy state, denoted by  $\circ$ , the HC cells are restricted to the centre of the domain. Outside the central region the large-scale flow is weak and disorganized: see [Figure 10\(c\)](#). Thus the noisy periodicity in kinetic energy corresponds to an expansion and contraction of the HC cells.

Despite some quantitative differences, most notably lower kinetic energy, the 3D flow with  $\ell_y/h = 1$  is similar to that of the 2D flow with  $\ell_y/h = 0$  (and the effectively 2D flow with  $\ell_y/h = 1/16$ ). The modest increase in  $\langle b_z \rangle$  indicates that the small additional dissipation  $\varepsilon$  introduced by three-dimensional motions remains secondary compared with the dominant boundary-layer dissipation. The restratification mechanism remains unchanged.

Three-dimensional simulations with  $\text{Ra}_V = 10^6$  and  $10^7$  showed the same qualitative behavior as for  $\text{Ra}_V = 10^8$  discussed above.

## 7. Conclusion

This study identifies the dynamical conditions under which bottom-heated fluids become restratified and shows that HC plays a central role in setting the global buoyancy structure. By linking the onset of restratification to the competition between vertical and horizontal buoyancy forcing, we provide a framework for predicting how global stratification develops and adjusts. Future work should extend this framework to include the effects of rotation, salinity, spatially inhomogeneous bottom heating and spherical geometry, which are essential ingredients for assessing restratification processes in subglacial oceans and lakes.

**Acknowledgements.** The authors thank Louis-Alexandre Coustou for discussion of this problem and the referees for their constructive comments, which improved the manuscript.

**Funding.** This research was supported by the Simons Foundation as part of the project *Fundamental Fluid Processes in Climate, Stellar, and Planetary Modeling*.

**Declaration of interests.** The authors report no conflict of interest.

**Author ORCID.** Florian Rein, <https://orcid.org/0009-0006-2060-7362>. Stefan Llewellyn Smith, <https://orcid.org/0000-0002-1419-6505>. William Roy Young, <https://orcid.org/0000-0002-1842-3197>.

## Appendix A. The geothermal flux Rayleigh number

As a typical geothermal heat flux,  $Q^{\text{gt}}$ , we use  $50 \text{ mW m}^{-2}$  (milliwatts per square meter), characteristic of abyssal-plane heat flux, but less than the global mean  $86.4 \text{ mW m}^{-2}$  estimated by Emile-Geay & Madec (2009). If  $Q^{\text{gt}}$  is transmitted vertically only by molecular diffusion of heat in water, with diffusivity  $\kappa$ , then the temperature gradient is

$$T_z^{\text{diff}} = \frac{Q^{\text{gt}}}{\kappa \rho c_p}. \quad (\text{A } 1)$$

In the denominator above  $\kappa \rho c_p$  is the thermal conductivity, denoted  $k$  in CNF. With  $\rho c_p \approx 4 \times 10^6 \text{ J m}^{-3} \text{ K}^{-1}$  and  $\kappa \approx 10^{-7} \text{ m}^2 \text{ s}^{-1}$ , the vertical temperature gradient in (A 1) is  $0.125 \text{ K m}^{-1}$ . With an ocean depth  $h \approx 5000 \text{ m}$  (characteristic of an abyssal plane) the implied vertical temperature difference between top and bottom is

$$\Delta T_V^{\text{diff}} = h T_z^{\text{diff}} = 625 \text{ K}. \quad (\text{A } 2)$$

Although the 50 milliwatts per square meter geothermal flux is smaller than ocean surface heat fluxes by a factor of  $10^3$  or  $10^4$ ,  $\Delta T_V^{\text{diff}} = 625 \text{ K}$  indicates that unopposed geothermal forcing is sufficient to produce strongly supercritical RBC.

Using  $\Delta T_V^{\text{diff}}$  motivates the definition of the flux Rayleigh number as

$$\text{Ra}_V = \frac{g \alpha \Delta T_V^{\text{diff}} h^3}{\nu \kappa} = \frac{g \alpha Q^{\text{gt}} h^4}{\rho c_p \nu \kappa^2} \approx 1.56 \times 10^{24}. \quad (\text{A } 3)$$

The numerical estimate in (A 3) uses  $h$  and  $\Delta T_V^{\text{diff}}$  above with  $\nu \approx 10 \kappa \approx 10^{-6} \text{ m}^2 \text{ s}^{-1}$ ,  $\alpha \approx 2 \times 10^{-4} \text{ K}^{-1}$  and  $g \approx 10 \text{ ms}^{-2}$ .

In the body of the paper we use a flux Rayleigh number  $\text{Ra}_V$  based on buoyancy flux  $F$ , with units  $\text{m}^2 \text{ s}^{-3}$ , rather than the geothermal heat flux  $Q^{\text{gt}}$ . The relation between these two fluxes is

$$F = \frac{g \alpha Q^{\text{gt}}}{\rho c_p}. \quad (\text{A } 4)$$

Using (A 4) to eliminate  $Q^{\text{gt}}$  from (A 3) produces the flux Rayleigh number  $\text{Ra}_V$  in (2.7).

## Appendix B. Numerical approach

### B.1. Numerical protocol and statistics

The governing equations (2.12–2.14) with boundary conditions (2.15) and no-slip conditions for each boundary, are solved numerically using *Nek5000* (Fischer 1997; Deville *et al.* 2002), which has been used extensively in thermal convection studies (e.g. Scheel *et al.* 2013; Rein *et al.* 2023). The domain is discretised using up to  $E = 2048$  elements which have been refined close to all boundaries to properly

resolve viscous and thermal boundary layers. The velocity is discretised within each element using Lagrange polynomial interpolants based on tensor-product arrays of Gauss–Lobatto–Legendre quadrature points. The polynomial order  $N$  on each element varies between 6 and 10 in this study. We use the 3/2 rule for dealiasing with extended dealiased polynomial order  $3N/2$  to compute nonlinear products. A third-order time stepping using a mixed explicit-implicit backward difference approach is used. A summary of the simulations physical and numerical parameters is provided in table 1.

We initialise all simulations with  $\mathbf{u} = 0$  and  $b = 0$ . Infinitesimal buoyancy perturbations of amplitude  $10^{-6}$  are introduced. Convection grows during a transient that typically lasts for  $t \approx h^2/\kappa$ , and which is longer as  $\Gamma$  increases. Once the system has reached a statistically-stationary state, various spatio-temporal averages are computed. We define the temporal and volume average operator  $\langle \rangle$  over the whole fluid domain volume  $V$  and over time  $t^*$  as

$$\langle A \rangle = \frac{1}{t^*V} \int_t^{t+t^*} \int_V A(\mathbf{x}, t) dV dt . \quad (\text{B1})$$

Typical  $t^*$  value range between  $100h^2/\kappa$  and  $h^2/\kappa$  for the lowest and the largest Rayleigh numbers respectively.

While most of the results discussed below are obtained using Direct Numerical Simulations (DNS), some extreme cases were only accessible via filtered simulations following the approach described in Fischer & Mullen (2001). To distinguish between DNS and filtered simulations, a viscous dissipation criterion has been used. A simulation with polynomial order  $N$  is considered to be a DNS when the time and volume averaged viscous dissipation  $\varepsilon$  varies by less than 5% when compared with the same simulation but using  $N + 2$  polynomial order. A simulation failing to satisfy this criteria is labelled as filtered and numerical stability is ensured by using a 1% filter on the last 2 polynomials (Fischer & Mullen 2001). Alternatively, one can use the criterion discussed in Scheel *et al.* (2013) which compares the isotropic Kolmogorov dissipative scale with the numerical grid size. For all the DNS simulations presented in this study, the numerical grid size is below the Kolmogorov dissipative scale.

### B.2. Summary of the simulation parameters

Table 1 provide all relevant numerical and physical parameters for the simulations performed using DNS or filtered approaches. Here,  $N$  denotes the polynomial order in both the  $x$  and  $z$  directions, and  $E$  is the total number of elements.

Table 1: Simulations summary (DNS or filtered) according to the physical and numerical parameters.

Ra <sub>V</sub>	Ra <sub>H</sub>	$\Gamma$	Ra <sub>H</sub> <sup>trad</sup>	Pr	DNS/filtered	E	N
0	[10 <sup>5</sup> , 10 <sup>6</sup> , 10 <sup>7</sup> , 10 <sup>8</sup> ]	8	5.12 × [10 <sup>7</sup> , 10 <sup>8</sup> , 10 <sup>9</sup> , 10 <sup>10</sup> ]	1	DNS	[512, 512, 1024, 1024]	10
10	[1.8, 2.643] × 10 <sup>2</sup>	8	[9.21, 13.53] × 10 <sup>4</sup>	1	DNS	256	6
10	2.75 × 10 <sup>2</sup>	12	4.75 × 10 <sup>5</sup>	1	DNS	256	6
10	[3.5, 4.6] × 10 <sup>2</sup>	16	[1.43, 1.88] × 10 <sup>6</sup>	1	DNS	256	6
10	[10, 6.5, 8.77] × 10 <sup>2</sup>	32	[3.28, 2.13, 2.87] × 10 <sup>7</sup>	1	DNS	256	6
30	10 <sup>3</sup>	32	3.28 × 10 <sup>7</sup>	1	DNS	256	6

Continued on next page

Table 1 – continued from previous page

$Ra_V$	$Ra_H$	$\Gamma$	$Ra_H^{\text{rad}}$	$Pr$	DNS/filtered	E	$N$
100	$[10^5, 10^6, 10^7, 10^8]$	8	$5.12 \times [10^7, 10^8, 10^9, 10^{10}]$	1	DNS	$[512, 512, 1024, 1024]$	10
100	$[6, 9.1] \times 10^2$	8	$[3.07, 4.66] \times 10^5$	1	DNS	256	6
100	$8.5 \times 10^2$	12	$1.47 \times 10^6$	1	DNS	256	6
100	$[11, 15] \times 10^2$	16	$[4.51, 6.14] \times 10^6$	1	DNS	256	6
100	$[10, 20.5, 28] \times 10^2$	32	$[3.28, 6.72, 9.18] \times 10^7$	1	DNS	256	8
300	$10^3$	32	$3.28 \times 10^7$	1	DNS	256	8
$10^3$	$[2.2, 3.69] \times 10^3$	8	$[1.13, 1.89] \times 10^6$	1	DNS	256	8
$10^3$	$2.75 \times 10^3$	12	$4.75 \times 10^6$	1	DNS	256	8
$10^3$	$[3.5, 5.2] \times 10^3$	16	$[1.43, 2.13] \times 10^7$	1	DNS	256	8
$10^3$	$[1, 6.6, 9.3] \times 10^3$	32	$[3.28, 21.6, 30.5] \times 10^7$	1	DNS	256	10
$10^3$	$[10, 30, 100, 300, 10^3]$	32	$[3.28 \times 10^5, 9.83 \times 10^5, 3.28 \times 10^6, 9.83 \times 10^6, 3.28 \times 10^7]$	1	DNS	256	10
$10^4$	$[0.95, 2.66] \times 10^4$	8	$[4.86, 13.6] \times 10^6$	1	DNS	256	8
$10^4$	$1.05 \times 10^4$	12	$1.81 \times 10^7$	1	DNS	256	8
$10^4$	$[1.25, 2.77] \times 10^4$	16	$[5.12, 11.35] \times 10^7$	1	DNS	256	8
$10^4$	$1.7 \times 10^4$	24	$2.35 \times 10^8$	1	DNS	512	8
$10^4$	$[2.2, 3.75] \times 10^4$	32	$[7.21, 12.3] \times 10^8$	1	DNS	512	10
$10^5$	100	8	$5.12 \times 10^4$	1	DNS	512	8
$10^5$	$[0, 0.735, 2.5] \times 10^5$	8	$[0, 3.76, 12.8] \times 10^7$	1	DNS	512	8
$10^5$	$0.75 \times 10^5$	12	$1.30 \times 10^8$	1	DNS	512	8
$10^5$	$[0.77, 2.48] \times 10^5$	16	$[3.15, 10.2] \times 10^8$	1	DNS	512	8
$10^5$	$0.85 \times 10^5$	24	$1.18 \times 10^9$	1	DNS	512	8
$10^5$	$[0.95, 2.46] \times 10^5$	32	$[3.11, 8.06] \times 10^9$	1	DNS	512	10
$10^6$	100	8	$5.12 \times 10^4$	1	DNS	512	10
$10^6$	$[0, 0.6, 2.25] \times 10^6$	8	$[0, 3.07, 11.5] \times 10^8$	1	DNS	512	10
$10^6$	$0.62 \times 10^6$	12	$1.07 \times 10^9$	1	DNS	512	10
$10^6$	$[0.61, 2.5] \times 10^6$	16	$[2.50, 10.24] \times 10^9$	1	DNS	512	10
$10^6$	$0.62 \times 10^6$	24	$8.57 \times 10^9$	1	DNS	1024	10
$10^6$	$[0.64, 2.45] \times 10^6$	32	$[2.10, 8.03] \times 10^{10}$	1	DNS	1024	10
$10^7$	100	8	$5.12 \times 10^4$	1	DNS	1024	10
$10^7$	$[0, 0.335, 2.03] \times 10^7$	8	$[0, 1.72, 10.4] \times 10^9$	1	DNS	1024	10
$10^7$	$0.35 \times 10^7$	12	$6.05 \times 10^9$	1	DNS	1024	10
$10^7$	$[0.35, 2.05] \times 10^7$	16	$[1.43, 8.40] \times 10^{10}$	1	DNS	1024	10
$10^7$	$0.35 \times 10^7$	24	$4.84 \times 10^{10}$	1	DNS	1024	10
$10^7$	$[0.1, 0.35, 2] \times 10^7$	32	$[3.28, 11.5, 65.5] \times 10^{10}$	1	DNS	1024	10
$10^8$	100	8	$5.12 \times 10^4$	1	DNS	1024	10
$10^8$	$[0, 0.2, 1.76] \times 10^8$	8	$[0, 1.02, 9.01] \times 10^{10}$	1	DNS	1024	10
$10^8$	$0.2 \times 10^8$	12	$3.46 \times 10^{10}$	1	DNS	1024	10
$10^8$	$[0.2, 1.7] \times 10^8$	16	$[8.19, 69.6] \times 10^{10}$	1	DNS	1024	10
$10^8$	$0.2 \times 10^8$	24	$2.76 \times 10^{11}$	1	DNS	2048	10
$10^8$	$[0.21, 1.7] \times 10^8$	32	$[6.88, 55.7] \times 10^{11}$	1	DNS	2048	10

Continued on next page

Table 1 – continued from previous page

$Ra_V$	$Ra_H$	$\Gamma$	$Ra_H^{\text{trad}}$	$Pr$	DNS/filtered	E	$N$
$10^9$	100	8	$5.12 \times 10^4$	1	filtered	2048	10
$10^9$	$[0, 0.14, 1.7] \times 10^9$	8	$[0, 7.17, 87.0] \times 10^{10}$	1	filtered	2048	10
$10^{10}$	$9 \times 10^8$	8	$4.61 \times 10^{11}$	1	filtered	2048	10
$10^7$	$3.35 \times 10^6$	8	$1.71 \times 10^9$	[2,3,4,6,7,8 10,11,12,13]	DNS	1024	10
$10^7$	$[3.19, 2.02] \times 10^6$	8	$[1.63, 1.03] \times 10^9$	4	DNS	1024	10
$10^7$	$[3.15, 1.96] \times 10^6$	8	$[1.61, 1.00] \times 10^9$	7	DNS	1024	10
$10^7$	$[3.1, 1.94] \times 10^6$	8	$[1.61, 0.99] \times 10^9$	10	DNS	1024	10
$10^7$	$[3.07, 1.93] \times 10^6$	8	$[1.57, 0.98] \times 10^9$	13	DNS	1024	10

### Appendix C. A large aspect ratio regime

We consider the non-dimensional governing equations (2.12)–(2.14) with the boundary conditions (2.15). We use the notation  $\epsilon = \Gamma^{-1} \ll 1$  and focus on the two-dimensional case with a streamfunction  $\psi$  such that  $(u, w) = (-\psi_z, \psi_x)$ . We eliminate the pressure to form the out-of-plane vorticity equation and define the rescaled horizontal coordinate  $X = \epsilon x$  and rescaled buoyancy and Rayleigh numbers

$$B = \epsilon b, \quad \hat{Ra}_V = \epsilon Ra_V, \quad \hat{Ra}_H = \epsilon Ra_H. \quad (\text{C } 1)$$

After these machinations, the steady equations of motion are

$$\begin{aligned} Pr^{-1} \epsilon [\psi_X (\epsilon^2 \psi_{XX} + \psi_{zz})_z - \psi_z (\epsilon^2 \psi_{XX} + \psi_{zz})_X] \\ = B_X + \epsilon^4 \psi_{XXXX} + 2\epsilon^2 \psi_{XXzz} + \psi_{zzzz}, \end{aligned} \quad (\text{C } 2)$$

$$\epsilon [\psi_X B_z - \psi_z B_X] = \epsilon^2 B_{XX} + B_{zz}, \quad (\text{C } 3)$$

with boundary conditions

$$B(X, 1) = -\hat{Ra}_H \tau(X), \quad B_z(X, 0) = -\hat{Ra}_V. \quad (\text{C } 4)$$

Above,  $\tau(X) = \cos(2\pi X)$  and  $-1/2 < X < 1/2$ .

With small  $\epsilon$  we can develop a lubrication-type approximation by considering the distinguished limit in which  $\epsilon \rightarrow 0$  with  $\hat{Ra}_H$  and  $\hat{Ra}_V$  fixed and order unity. Our objective is to compute the two-dimensional steady-state solution for Rayleigh numbers sufficiently small to remain below the threshold for any instability. We seek a solution of (C2) and (C3) for the streamfunction and the rescaled buoyancy expanded in powers of  $\epsilon$  as

$$\begin{aligned} B(X, z) &= B_0(X, z) + \epsilon B_1(X, z) + \dots, \\ \psi(X, z) &= \psi_0(X, z) + \epsilon \psi_1(X, z) + \dots. \end{aligned} \quad (\text{C } 5)$$

Substituting these expansions into (C2) and (C3) gives at leading order

$$B_{0zz} = 0 \quad \text{and} \quad \psi_{0zzzz} = -B_{0X}. \quad (\text{C } 6)$$

The solution of the buoyancy equation satisfying the the top and bottom boundary conditions (C4) is

$$B_0(X, z) = \hat{Ra}_V (1 - z) - \hat{Ra}_H \tau(X). \quad (\text{C } 7)$$

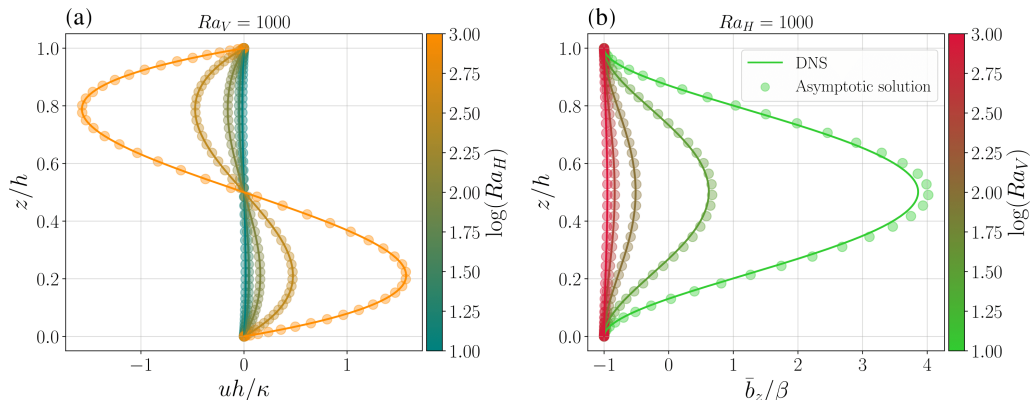


Figure 12: (a) Vertical profile of the horizontal velocity at  $X = 1/2$  for  $Ra_H \in [10, 30, 100, 300, 1000]$  for fixed  $Ra_V = 1000$ . (b) Vertical profile of  $\bar{b}_z$  for  $Ra_V \in [10, 30, 100, 300, 1000]$  for a fix  $Ra_H = 1000$ . The continuous lines (—) represent the DNS data and circles (o) represent the asymptotic solution ((C8) for (a) and based on (C7),(C10) for (b)). The input parameters are  $\Gamma = 32$  and  $Pr = 1.0$ .

We can then solve the vorticity equation in (C6) to find

$$\psi_0(X, z) = \hat{Ra}_H P(z) \tau_X, \quad \text{with} \quad P(z) = \frac{z^2(1-z)^2}{24}. \quad (\text{C8})$$

The polynomial  $P(z)$  is defined by  $P^{(IV)} = 1$ , with  $P(0) = P'(0) = P(1) = P'(1) = 0$ . The leading-order buoyancy field,  $B_0(X, z)$  in (C7), is unaffected by the flow, i.e. there is no feedback from the velocity field on the buoyancy profile. To capture the first-order correction due to advection, we analyze the buoyancy equation at order  $O(\epsilon)$ ,

$$B_{1zz} = \psi_{0X} B_{0z} - \psi_{0z} B_{0X} = (\psi_0 B_{0z})_X - (\psi_0 B_{0X})_z. \quad (\text{C9})$$

Integrating (C9) twice in  $z$  gives

$$B_1 = -\hat{Ra}_V \hat{Ra}_H \tau_{XX} Q_0(z) + \hat{Ra}_H^2 \tau_X^2 Q_1(z), \quad (\text{C10})$$

with

$$Q_0(z) = \frac{z^6}{720} - \frac{z^5}{240} + \frac{z^4}{288} - \frac{1}{1440}, \quad (\text{C11})$$

$$Q_1(z) = \frac{z^5}{120} - \frac{z^4}{48} + \frac{z^3}{72} - \frac{1}{720}. \quad (\text{C12})$$

Polynomials  $Q_0(z)$  and  $Q_1(z)$  are defined by  $Q_0'' = P$  and  $Q_1' = P$ , with  $Q_1(1) = Q_0(1) = Q_0'(0) = 0$ , satisfying the buoyancy boundary conditions.

Figure 12 compares the vertical profiles of  $\bar{b}_z$  and the horizontal velocity obtained from a DNS with the approximate asymptotic solution derived earlier for several  $Ra_H$  at  $Ra_V$  ranging from 1 to 1000. The asymptotic solution neglects sidewall effects. Thus we use a large aspect ratio,  $\Gamma = 32$ , to minimize the influence of lateral boundaries in the bulk region. Overall, the asymptotic solution shows good agreement with the DNS results for both the buoyancy gradient and velocity fields.

Figure 12(b) shows that when  $Ra_V \approx Ra_H$  the flow is negatively stratified

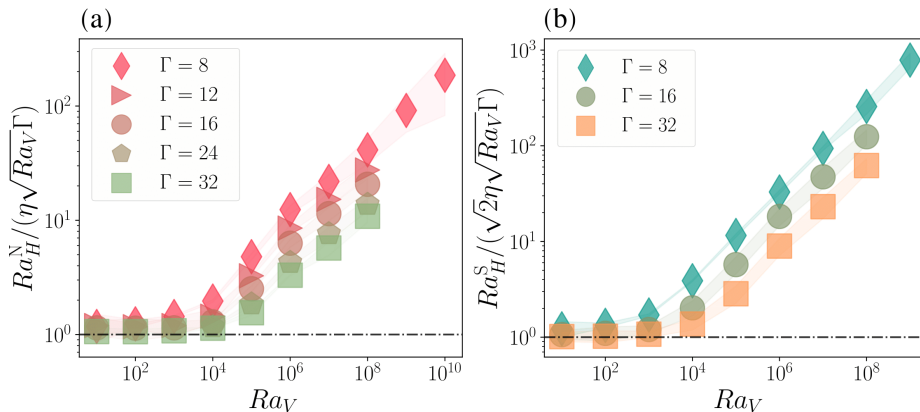


Figure 13: Neutral and strong horizontal Rayleigh numbers, (a)  $Ra_H^N$  and (b)  $Ra_H^S$ , compensated by their respective theoretical scalings in (C15) and plotted against the vertical Rayleigh number  $Ra_V$  for several aspect ratios  $\Gamma$ .

throughout the depth. Conversely, when  $Ra_V \ll Ra_H$  the bulk of the layer exhibits positive stratification. For fixed  $Ra_V$ , increasing  $Ra_H$  strengthens this stable stratification and extends it over a larger fraction of the depth, so that the domain as a whole can become positively stratified in a volume-mean sense. The condition at which the system first achieves positive mean stratification can be predicted from the lubrication solution derived above.

Using equations (C7) and (C10) and taking derivatives with respect to  $z$ , the vertical buoyancy gradient can be expressed as

$$b_z = -Ra_V + \epsilon^2 \left[ -Ra_V Ra_H \tau_{XX} Q'_0 + Ra_H^2 \tau_X^2 Q'_1 \right]. \quad (\text{C13})$$

The global average of (C13) is

$$\langle b_z \rangle = -Ra_V + \left( \frac{\epsilon Ra_H}{\eta} \right)^2, \quad (\text{C14})$$

where  $\eta^2 = -1/(Q_1(0)\overline{\tau_X^2}) \approx 36.5$  is a numerical constant resulting from the global averaging of the vertical and horizontal profiles of (C13). Examining the condition under which (C14) vanishes and/or reverse the imposed bottom flux provides insight into the scaling of neutral and strong stratification in the low Rayleigh regime. Setting  $\langle b_z \rangle = 0$  and  $\langle b_z \rangle = Ra_V$  gives respectively,

$$Ra_H^N = \eta \sqrt{Ra_V} \Gamma \quad \text{and} \quad Ra_H^S = \sqrt{2} \eta \sqrt{Ra_V} \Gamma. \quad (\text{C15})$$

In Figure 13, we show  $Ra_H^N$  and  $Ra_H^S$  compensated by their respective scaling relations (C15), plotted as a function of  $Ra_V$ . The results exhibit consistent trends, confirming the predicted  $Ra_V$ - and  $\Gamma$ -dependence in the low-Rayleigh-number regime, i.e. for  $Ra_V$  and  $Ra_H \lesssim 10^3$ . Furthermore, the relation (C15) also captures the prefactor with reasonable accuracy, although a slight deviation from the data is noticeable. Improving the quantitative agreement would require evaluating the  $O(\epsilon^2)$  correction to the buoyancy field. We conclude by noting that (C15) does not involve  $Pr$ .

## REFERENCES

- ASHKENAZY, Y. & TZIPERMAN, E. 2016 Variability, instabilities, and eddies in a snowball ocean. *Journal of Climate* **29**, 869–888.
- BIRE, S., KANG, W., RAMADHAN, A., CAMPIN, J.-M. & MARSHALL, J. 2022 Exploring ocean circulation on icy moons heated from below. *J. Geophys. Res.: Planets* **127**, e2021JE007025.
- COUSTON, L.-A., NANDAHA, J. & FAVIER, B. 2022 Competition between Rayleigh–Bénard and horizontal convection. *J. Fluid Mech.* **947**, A13.
- COUSTON, L.-A. & SIEGERT, M. 2021 Dynamic flows create potentially habitable conditions in Antarctic subglacial lakes. *Science Advances* **7**, eabc3972.
- DE LAVERGNE, C., MADEC, G., LE SOMMER, J., NURSER, A. J. G. & NAVEIRA GARABATO, A. C 2016 On the consumption of Antarctic Bottom Water in the abyssal ocean. *J. Phys. Oceanogr.* **46**, 635–661.
- DEVILLE, M. O., FISCHER, P. F. & MUND, E. H. 2002 *High-Order Methods for Incompressible Fluid Flow*. Cambridge, UK: Cambridge University Press.
- DOERING, CHARLES R 2020 Turning up the heat in turbulent thermal convection. *Proceedings of the National Academy of Sciences* **117** (18), 9671–9673.
- EMILE-GEAY, J. & MADEC, G. 2009 Geothermal heating, diapycnal mixing and the abyssal circulation. *Ocean Science* **5**, 203–217.
- FISCHER, P. & MULLEN, J. 2001 Filter-based stabilization of spectral element methods. *C. R. Acad. Sci. I Math.* **332**, 265–270.
- FISCHER, P. F. 1997 An overlapping Schwarz method for spectral element solution of the incompressible Navier–Stokes equations. *J. Comp. Phys.* **133**, 84–101.
- GERKEMA, T., ZIMMERMAN, J. T. F., MAAS, L. R. M & VAN HAREN, H. 2008 Geophysical and astrophysical fluid dynamics beyond the traditional approximation. *Rev. Geophys.* **46**.
- GOLUSKIN, D. 2016 *Internally heated convection and Rayleigh–Bénard convection*. Cham, Switzerland: Springer.
- GROSSMANN, S. & LOHSE, D. 2000 Scaling in thermal convection: a unifying theory. *J. Fluid Mech.* **407**.
- GROSSMANN, S. & LOHSE, D. 2001 Thermal convection for large Prandtl numbers. *Phys. Rev. Lett.* **86**, 3316–3319.
- HOFFMAN, P. F & SCHRAG, D. P 2002 The snowball Earth hypothesis: testing the limits of global change. *Terra Nova* **14**, 129–155.
- HUGHES, G. O. & GRIFFITHS, R. W. 2008 Horizontal convection. *Annu. Rev. Fluid Mech.* **40**, 185–208.
- JANSEN, M. F. 2016 The turbulent circulation of a Snowball Earth ocean. *J. Phys. Oceanogr.* **46**, 1917–1933.
- JOHNSTON, H. & DOERING, C. R. 2009 Comparison of turbulent thermal convection between conditions of constant temperature and constant flux. *Phys. Rev. Lett.* **102**, 064501.
- LEMASQUERIER, D. G., BIERSON, C. J. & SODERLUND, K. M. 2023 Europa’s ocean translates interior tidal heating patterns to the ice-ocean boundary. *AGU Advances* **4**, e2023AV000994.
- LINDBORG, ERIK 2023 Scaling in Rayleigh–Bénard convection. *Journal of Fluid Mechanics* **956**, A34.
- MULLARNEY, J. C., GRIFFITHS, R. W. & HUGHES, G. O. 2006 The effects of geothermal heating on the ocean overturning circulation. *Geophys. Res. Lett.* **33**.
- MUNK, W. & WUNSCH, C. I. 1998 Abyssal recipes II: energetics of tidal and wind mixing. *Deep Sea Res. Part I* **45**, 1977–2010.
- OTERO, J., WITTENGER, R. W., WORTHING, R. A. & DOERING, C. R. 2002 Bounds on Rayleigh–Bénard convection with an imposed heat flux. *Journal of Fluid Mechanics* **473**, 191–199.
- PAPARELLA, F. & YOUNG, W. R. 2002 Horizontal convection is non-turbulent. *J. Fluid Mech.* **466**, 205–214.
- PASSAGGIA, PY, COHEN, N. F. & SCOTTI, A. 2024 Limiting regimes of turbulent horizontal convection. part 2. large prandtl numbers. *Journal of Fluid Mechanics* **997**, A6.

- PASSAGGIA, PY & SCOTTI, A. 2024 Limiting regimes of turbulent horizontal convection. part 1. intermediate and low prandtl numbers. *Journal of Fluid Mechanics* **997**, A5.
- PIERREHUMBERT, R. T., ABBOT, D. S., VOIGT, A. & KOLL, D. 2011 Climate of the Neoproterozoic. *Ann. Rev. Earth Planetary Sci.* **39**, 417–460.
- REIN, F., CARÉNINI, L., FICHOT, F., FAVIER, B. & LE BARS, M. 2023 Interaction between forced and natural convection in a thin cylindrical fluid layer at low Prandtl number. *J. Fluid Mech.* **977**, A26.
- ROCHA, C.B., CONSTANTINOU, N.C., LLEWELLYN SMITH, S. G. & YOUNG, W.R. 2020 The Nusselt numbers of horizontal convection. *Journal of Fluid Mechanics* **894**, A24.
- ROSSBY, H. T. 1965 On thermal convection driven by non-uniform heating from below: an experimental study. *Deep Sea Res.* **12**, 9–16.
- ROSSBY, H. T. 1998 Numerical experiments with a fluid heated non-uniformly from below. *Tellus A* **50**, 242–257.
- SCHEEL, J. D., EMRAN, M. S. & SCHUMACHER, J. 2013 Resolving the fine-scale structure in turbulent Rayleigh-Bénard convection. *New J. Phys.* **15**, 113063.
- SHISHKINA, O., GROSSMANN, S. & LOHSE, D. 2016 Heat and momentum transport scalings in horizontal convection. *Geophys. Res. Lett.* **43** (3), 1219–1225.
- SODERLUND, K. M. 2019 Ocean dynamics of outer solar system satellites. *Geophys. Res. Lett.* **46**, 8700–8710.
- THOMA, M., GROSFELD, K., FILINA, I. & MAYER, C. 2009 Modelling flow and accreted ice in subglacial Lake Concordia, Antarctica. *Earth Planetary Sci. Lett.* **286**, 278–284.
- WANG, F., HUANG, S.-D., ZHOU, S.-Q. & XIA, K.-Q. 2016 Laboratory simulation of the geothermal heating effects on ocean overturning circulation. *J. Geophys. Res.: Oceans* **121**, 7589–7598.
- WINTERS, K.B. & YOUNG, W. R. 2009 Available potential energy and buoyancy variance in horizontal convection. *Journal of Fluid Mechanics* **629**, 221–230.
- WUNSCH, C. 2016 Tides of global ice-covered oceans. *Icarus* **274**, 122–130.
- WUNSCH, C. & FERRARI, R. 2004 Vertical mixing, energy, and the general circulation of the oceans. *Annu. Rev. Fluid Mech.* **36**, 281–314.
- ZHANG, Y., KANG, W. & MARSHALL, J. 2024 Ocean weather systems on icy moons, with application to Enceladus. *Science Advances* **10**, 6857.